Masteroppgave

NTNU
Norges teknisk-naturvitenskapelige universitet
Fakultet for naturvitenskap
Institutt for kjemi

Tage Winther Maltby

A Study of the Entropy Production in Liquid Phase Shock Waves

Masteroppgave i Industriell kjemi og bioteknologi
Veileder: Øivind Wilhelmsen
Januar 2022

NTNU
Kunnskap for en bedre verden

Tage Winther Maltby

A Study of the Entropy Production in Liquid Phase Shock Waves

Masteroppgave i Industriell kjemi og bioteknologi
Veileder: Øivind Wilhelmsen
Januar 2022

Norges teknisk-naturvitenskapelige universitet
Fakultet for naturvitenskap
Institutt for kjemi

NTNU
Kunnskap for en bedre verden

A Study of the Entropy Production in Liquid Phase Shock Waves

Author: Tage Winther Maltby
Supervisor: Professor Øivind Wilhelmsen

Norwegian University of Science and Technology
Norway
Spring 2022

Acknowledgements

Throughout this thesis work I have gotten wonderful assistance, challenges and guidance, which has taught me great lessons and inspired me.

I would first like to thank my supervisor, Professor Øivind Wilhelmsen, for his guidance, patience, and tremendous insight, challenging what I know and motivating me to improve my work. I would like to thank Bjørn Hafskjold for guiding me through the use of Non-Equilibrium Molecular Dynamics (NEMD) and for great discussions regarding the properties of shock waves. I would also like to thank Dick Bedeaux, Signe Kjelstrup, Morten Hammer, and Magnus Aashammer Gjennestad for their time and insights regarding Non-Equillibrium Thermodynamics and numerical modeling. I would also like to acknowledge the facilites at Porelab for being a calming and vitalizing place of work.

Abstract

In this thesis we have simulated a liquid shock wave using Non-Equilibrium Molecular dynamic (NEMD) simulations and the Navier-Stokes (N-S) equations. The new application of the N-S equations combined an Equation of state (EOS) for the Lennard-Jones/spline (LJ/s) fluid, a transport coefficient equation for argon, the spatial FORCE flux, and an ordinary differential equation (ODE) integrator to solve a transient shock. The methodologies both yielded similar profiles, but with some characteristic differences. The N-S equations had a sharper shock front, a lower measurable heat flux and a lower temperature in the boundary layer. The sharper shock front, compared to NEMD and experimental methods, has been a characteristic of the N-S equations in previous work.

By utilizing the simulation data, shock wave properties were calculated. First, the shock wave position was determined using the definition of the Gibbs equimolar surface. The speed of sound was determined to be $v^*_{sound} = 4.7$ using the EOS, the Mach number was computed for both methods, and showed that the wave was moving at $M \approx 2$. The Excess internal energy- and entropy density were determined and the surface temperatures were found to be $T^{s*}_{N-S} = 3.2$ for the N-S equations and $T^{s*}_{NEMD} = 2.82 \pm 0.184$ for the NEMD simulations.

The excess entropy production of the liquid shock wave was determined using five different methods, including a newly developed method named the Macro Entropy Method (MEM). All of the methods yielded similar results using the N-S equations, whereas the methods would differ more for the NEMD simulations. It was also observed that the N-S equations had a similar excess entropy production to the NEMD simulations, even when the N-S equations did not include bulk viscous contributions. This was discussed in detail, some of the main points being the dissipation in the FORCE flux, sharpness of the shock front, the accuracy of the EOS, the assumption of local equilibrium and the size of the NEMD simulations.

To check the accuracy of the EOS, the EOS functions for pressure, internal energy and enthalpy were compared with NEMD data which showed that the EOS underestimated the properties in the shock front, likely due to the assumption of local equilibrium. Uncertainty of the position of the shock front and computation of error bars were also reviewed.

Sammendrag

Vi har simulert en sjokkbølge i væskefase ved bruk av Non-Equilibrium Molecular dynamics (NEMD) og Navier-Stokes (N-S) ligningene. Den nye anvendelsen av N-S ligningene kombinerte en tilstandslikning (EOS) for et Lennard-Jones/spline (LJ/s) fluid, en transportkoeffisientligning for argon, den romlige FORCE-fluksen og en ordinær differensialligning (ODE) integrator for å løse et dynamisk sjokk. De to metodene ga lignende profiler, men hadde noen karakteristiske forskjeller. N-S likningene hadde en skarpere sjokkfront, lavere målbar varmefluks og lavere temperatur der sjokket ble skapt. Den skarpere sjokkfronten, sammenlignet med NEMD og eksperimentelle metoder, har vært karakteristisk for N-S-ligningene i tidligere arbeid.

Ved å utnytte simuleringsdataene ble sjokkbølgeegenskaper funnet. Først ble posisjonen til sjokkbølgen bestemt ved å bruke definisjonen av Gibbs ekvimolare overflate. Lydhastigheten ble bestemt til å være $v^*_{sound} = 4.7$ ved bruk av tilstandslikningen. Machtallet ble beregnet for begge metodene, og viste at bølgen beveget seg med $M \approx 2$. Excess indre energi- og entropitetthet ble bestemt og overflatetemperaturene ble bestemt til å være $T^{s*}_{NS} = 3.2$ for N-S ligningene og $T^{s*}_{NEMD} = 2.82 \pm 0.184$ for NEMD-simuleringene.

Excess entropiproduksjon av sjokkbølgen ble bestemt ved hjelp av fem forskjellige metoder, inkludert en nyutviklet metode kalt Macro Entropy Method (MEM). Alle metodene ga lignende resultater ved bruk av N-S ligningene, mens metodene fluktuerte mer for NEMD-simuleringene. Det ble også observert at N-S ligningene hadde en lignende excess entropiproduksjon som NEMD-simuleringene, selv om N-S-ligningene ikke inkluderte bulkviskositet. Dette ble diskutert i detalj, der noen av hovedpunktene var dissipasjon på grunn av FORCE-fluksen, skarpheten til sjokkfronten, nøyaktigheten til EOSen, antakelsen om lokal likevekt og størrelsen på NEMD-simuleringene.

For å sjekke nøyaktigheten til tilstandslikningen ble EOS-funksjonene for trykk, intern energi og entalpi sammenlignet med NEMD-data. Dette viste at EOS undervurderte egenskapene i sjokkfronten, sannsynligvis på grunn av antakelsen om lokal likevekt. Usikkerhet rundt posisjonen til sjokkfronten og beregning av usikkerhet ble også gjennomgått.

Table of Contents

List of Figures

List of Symbols and Units

a	Helmholtz free energy	J
a^{res}	Residual Helmholtz free energy	J
B	Virial coefficient	$\mathrm{m}^3/\mathrm{mole}$
C_p	Heat capacity at constant pressure	J/mole
C_v	Heat capacity at constant volume	J/mole
E, E_i	Total energy, Total energy of particle i	J
$\mathbf{F}_i$	Force acting on particle i	N
H, h	Enthalpy, Specific enthalpy	J, J/kg
$\mathbf{J}, j$	Mass flux	$\mathrm{kg}/\mathrm{m}^2\mathrm{s}$
$\mathbf{J}_q^{'}, J_q^{'}$	Measurable heat flux	$\mathrm{J}/\mathrm{m}^2\mathrm{s}$
J_s	Entropy flux	$\mathrm{J}/\mathrm{Km}^2\mathrm{s}$
k	Boltzman constant	J/K
L	Cell length	m
L_x, L_y, L_z	Cell length in direction α	m
l	Surface position	m
M	Mach number	-
M_m	Molar mass	kg/mol
m_i	Mass of particle i	kg
N	Number of particles	-
N_a	Avogadros Number	mol^{-1}
r_c	Cut-off radius	m
$\mathbf{r}_i, r_{ij}$	Position of particle i, Distance between particle i and j	m
r_s, r_{spline}	Spline radius	m
P, p	Pressure tensor, Pressure	Pa
$\mathbf{p}_i$	Momentum of particle i	Ns
s	Specific entropy	J/kgK
T	Temperature	K
T^s	Surface temperature	K
T_c	Critical temperature	K
u	Specific internal energy	J/kg
U, u_{pot}	Potential energy	J

V	Volume	m^3
$v, \mathbf{v}_i$	Fluid velocity, speed of particle i	m/s
v_{sound}	Speed of sound	m/s
v^s	Speed of surface	m/s
ϵ	Minimum potential energy	J
ϵ_{ij}	Minimum potential energy between particle i and j	J
ζ	Bulk viscosity	kg/ms
η	Shear viscosity	kg/ms
κ	Thermal conductivity	W/Km
μ^s	Chemical potential of surface	J
Π	Viscous pressure tensor	Pa
ρ	Density	kg/m^3
ρ_c	Critical density	kg/m^3
ρ_s	Number entropy density	J/Km^3
ρ_u	Number internal energy density	J/m^3
σ_s	Entropy production	$\mathrm{J}/\mathrm{sKm}^3$
σ_s^s	Excess entropy production	$\mathrm{J}/\mathrm{sKm}^2$
Ω	Collision integral	-

Chapter 1

Introduction

A shock wave is a sudden, almost discontinuous change in temperature, pressure and density travelling at supersonic speed [2]. Shock waves are highly irreversible and the amount of energy carried by the wave is substantial. They are therefore often generated in explosions like those from IEDs (improvised explosive devices), lightning or objects moving faster than the speed of sound, such as jet planes or bullets. The phenomenon has been of interest in several fields due to its applications and destructive properties. Shock waves have been utilized in medicine, where they can disintegrate kidney stones [3] and in the industry, where shock waves are used in processes such as explosive welding and sandal wood oil extraction [4]. They are also highly relevant in aerodynamics, where the study of shock-wave phenomena are one of the most important aspects of understanding supersonic flows [2]. Thus, understanding the behavior of the shock wave and its almost discontinuous profiles could benefit a vast array of scientific fields. Understanding how energy is converted and entropy produced in a shock wave could prove vital, for example in medicine, where carelessly applied shock waves were shown to damage hips and potentially damage large vessels and nerves[3].

Shock waves have been has analysed extensively in the fields of physics before, this recount will therefore limit itself to a more general history of shock waves and focus on research that have utilized the Navier-Stokes (N-S) equations and Molecular dynamic (MD) simulations. We start with Ernst Mach. Mach was the first to photograph a speeding bullet in 1887 [1], capturing an image of the shock front. He was the first to recognize the real nature of shock waves in air and his subsequent research would access a new field in physics, the field of supersonic flow of gases [5]. The Rankine-Huginot conditions, developed in the late 19th century, managed to describe the conditions for a shock wave in one dimension [6, 7]. By considering a dissipative fluid, a shock wave was treated as a surface of discontinuity where mass, momentum and energy were conserved [8]. In the Rankine-Huginot conditions the shock properties were described in terms of the properties before (upfront) and behind (downstream) the shock front, these equations gave a macroscopic description of the shock wave, but did not describe details like energy dissipation in the shock front. Details about the shock front were expanded upon in the 20th century by the use of hydrodynamic theories. Work by Becker managed to determine the shock wave thickness while Jouget and Chapman found that a detonation wave is compromised of a supersonic shock wave followed by a sonic combustion wave [8, 9, 10, 11]. There was a peaked interest for shock waves during and after the second world war, which led to significant progress in the understanding of gaseous and liquid shock

waves e.g. the work by Friedlander[12] on the diffraction effects of planar sound pulses, for work done during world war 2 and after see Chapter 3 Krehl [13] for a chronological review which stretches to the early 00s.

Throughout the study of shock waves, researchers have utilized the conservative equations [13], which are equations describing the conservation of mass, momentum and energy. An extension of the conservative equations, the Navier-Stokes equations, which include viscous and conductive contributions [14], was first implemented by Becker on non-weak shock waves in 1921 [9]. The Navier-Stokes equations have since then been utilized and discussed to a significant degree, work done using the equations found that the thickness of the shock front was thinner compared to experimental data [15], and questions regarding the consistency between the entropy profile and the second law of thermodynamics were raised [16]. A proposed improvement to the N-S equations have been the Burnett equations [13]. Work by Pham-Van-Diep and coworkers found that when comparing the Navier-Stokes equations to the Burnett equations, the latter was more accurate for higher Mach numbers [17]. In addition, work modelling transient shocks found the Burnett equations predicted better results, although the methods were found to be numerically unstable for fine meshes [18]. With the expansion of computational fluid dynamics (CFD), transient shocks could be modelled numerically using the Navier-Stokes equations [14, 19]. The field has led to the development of numerous methods e.g. stable centered numerical differencing methods, such as the FORCE and WENO flux which can be used to solve discontinuous phenomena [19, 20]. With the field of available techniques, CFD has provided new insight and has already been applied to complex phenomena such as the modelling of bubble collapse and multi-phase flows with the presence of shock waves [21, 22].

Moving to the mid-20th century, another computational method proved useful for the study of shock waves. Shock waves, being incredibly fast phenomena, could be analyzed using molecular dynamic (MD) simulations. Shock wave simulations were first performed in one dimension in 1966 by Tsai and Becket [23], then at the start of the 1970s simulations were expanded to a three dimensional Lennard-Jones system and subsequently to a Lennard-Jones fluid in the late 70s and early 80s [24]. MD simulations, together with Direct Simulation Monte Carlo (DSCM) methods, provided a connection between experimental and theoretical methods [15], the exact thickness of the shock front was determined by Hoover [25] in 1979. Subsequent work compared Non-Equilibrium Molecular dynamic (NEMD) simulations with the Navier-Stokes equations where it was found that the N-S equations described shock waves reasonably well, although the shock front was found to be thinner [26]. DSCM methods have been in good agreement with NEMD simulations. Comparisons between DSCM, NEMD, and the Navier-Stokes equations found that DSCM and NEMD gave nearly identical results while the N-S profiles had a narrower shock front once more [27]. Holian, intrigued by the results, investigated whether the discrepancy between the N-S equations and other simulation methods could be solved by using the temperature in the direction of shock propagation T_{xx}, instead of the average temperature, and found the results to agree better with the NEMD and DSCM data, thus finding a possible reason for the N-S equations having thinner gradients [24, 28]. NEMD simulations are highly accurate but the method has limitations e.g. only being able to simulate systems for a few nanoseconds and requiring large systems to simulate gases. This is not necessarily a problem when studying shock waves due to their speed, but it does limit NEMD to smaller systems and longer calculation times [29, 24].

Even with the large amount of research done on shock waves there are still aspects of the shock wave left to explore. In an article by Hafskjold and coworkers it was pointed out there were few papers concerned with the energy dissipation and entropy production

of shock waves, even when the phenomenon is known to be highly irreversible, thus, they investigated these features using NEMD simulations of a gaseous Lennard-Jones/spline fluid (LJ/s) [30]. In addition to computing shock position, speed and surface temperature, four different methods for computing the excess entropy were used, two of them used the local entropy production and two considered the shock front as a surface of discontinuity. The methods were found to be in good agreement, though the methods using the surface of discontinuity were deemed to be more robust. Since the article was published, van Westen and Coworkers have developed a new equation of state (EOS) for the LJ/s fluid. Known as the uv-Theory, the EOS has shown excellent agreement with NEMD results compared to other perturbation theories [31]. The EOS can be accessed and utilized with the Python module Thermopack to compute properties such as internal energy, entropy and pressure [32].

Access to the in-house NEMD code by Hafskjold and the new EOS for the LJ/s fluid presented new opportunities which this thesis work has explored. The first was to simulate a shock wave in a liquid phase LJ/s fluid using NEMD and, with the help of the EOS, derive the surface properties and compute the entropy production of the liquid shock. This was done to investigate whether the methods used for the gas phase shock would hold for the liquid phase. The second opportunity was to independently model a transient liquid shock wave using the Navier-Stokes equations with the new EOS, a stable numerical flux known as the FORCE flux, and an Ordinary Differential Equation (ODE) integrator. This was done to make a comparative analysis between the NEMD and N-S equations and test whether the methods for determining shock properties and entropy production would work with a continuous description. In addition to the main goals, we developed another method for determining the excess entropy production called the Macro Entropy Method (MEM), tested the agreement between NEMD and the uv-theory for internal energy, enthalpy and pressure, and investigated the error analysis of the NEMD simulations.

The thesis is split into the following Sections: theory, method, results and discussion, conclusion and future work. In the theory section the relevant theory will be reviewed, starting with general theory shock waves, we move to the necessary equations in NEMD and the formulation of the N-S equations and end with theories utilized in both methods i.e., the determination of excess- and transport properties and methods for determining the entropy production. The method section is shaped similarly to the theory section but will focus on the implementation of the theories mentioned using computational methods. The results section will compare the two methods starting with the general profiles of temperature, pressure, fluid velocity, and density. Then a comparison of shock position and speed followed by a comparison of excess properties and surface temperature. Once the surface properties have been computed we present the entropy production methods one at a time and end with a comparison of all the methods. In addition, we will look at the agreement between NEMD and the uv-theory and investigate the error analysis of NEMD. Lastly, the conclusion and future work will be summarizing the work done and contain a discussion of new avenues for future research, such as the modelling of gas phase LJ/s fluid, testing other numerical fluxes, and implementing contributions such as the bulk viscosity.

Chapter 2

Theory

2.1 General shock wave theory

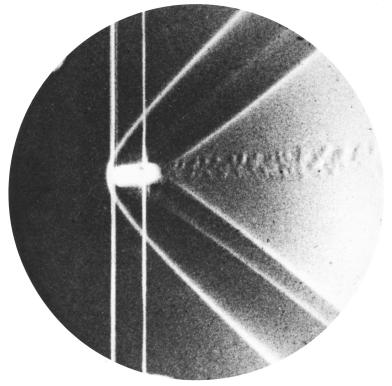

Figure 2.1: A picture of a bullet surrounded by a white parabole shock wave [1].

A shock wave is characterized by a pressure-dependent, supersonic velocity of propagation and the formation of a steep wave front with abrupt changes in all its thermodynamic quantities [8]. It has a sharp and almost discontinuous change in temperature, pressure and density. Figure 2.1 shows a bullet passing through the air generating a shock wave, the wave front is the white parabolic line in front of the bullet and the two straight lines behind it. The wave front is the area where the sudden change in stress, density, and temperature is located.

When working with shock waves it is useful to have knowledge of a certain dimensionless number and fluid properties. These are the Mach number and the speed of sound respectively. The speed of sound is the distance travelled per unit of time by a sound wave which is propagated by molecular collisions [2]. This property depends on temperature and the medium through which the sound wave propagates. For example, in regular air the speed of sound is around 343 m/s [33], but in water the speed of sound is 1500 m/s [34]. In terms of the thermodynamic properties, the speed of sound can be defined as:

$$v_{sound}^2 = \frac{C_p}{C_v}\left(\frac{\partial p}{\partial \rho}\right)_T \tag{2.1}$$

where p is the pressure while C_p and C_v are the heat capacities at constant pressure and volume respectively [30]. Knowing the speed of sound can give information on the heat capacities and it enables us to calculate the Mach number.

The Mach number is a dimensionless number represented by the ratio of a local velocity v to the speed of sound v_{sound}.

$$M = \frac{v}{v_{sound}} \tag{2.2}$$

Knowing the Mach number of a shock wave gives information about how fast and how strong it is e.g. if a shock wave has a Mach number which is larger than 1, the shock is moving at supersonic speeds, meaning it will move faster than the speed of sound [2].

2.2 Non-Equilibrium Molecular Dynamics Simulations of a blast

Non-Equilibrium Molecular Dynamics (NEMD) Simulations is a computer technique designed to study transport processes. It does this by solving the Newton's equation of motion for particles in a system. The particles will collide with each other and the systems walls, subsequently the transport properties are calculated from the mechanical properties from that set of colliding particles. In this project we will utilize boundary driven NEMD, where gradients are applied to a system by perturbation of its boundaries [35].

The considered system may consist of a number of particles N in a rectangular box of volume $V = L_x L_y L_z$. The volume is determined by setting the molar density as:

$$\rho = V\frac{N_A}{N} = L_x L_y L_z \frac{N_A}{N} \tag{2.3}$$

where N_A is Avogadros number. Typically, these simulations are used to determine transport properties in the x-direction so the axial length is larger than the lateral lengths i.e. $L_x > L_y = L_z$. Each of the particles within this box will have a pair potential with the other particles. Particles that are to close will repel each other while those distant will attract each other. The pair potential NEMD utilizes to describe this is the Lennard-Jones/spline potential which is based on the Lennard-Jones potential[35]:

$$u_{ij} = 4\epsilon_{ij}\left[\left(\frac{\sigma_{ij}}{r_{ij}}\right)^{12} - \left(\frac{\sigma_{ij}}{r_{ij}}\right)^{6}\right] \tag{2.4}$$

Where u_{ij} is the potential between a particle i and j, ϵ_{ij} is the minimum potential between the particles, r_{ij} is the distance between the particles and σ_{ij} is the distance between the particles when the potential is equal to zero.

For the Lennard-Jones/spline potential, which is more time efficient compared to the Lennard-Jones potential, the pair potential is set to zero for particles that are a certain distance from each other $r > r_c$. Unlike cut-off Lennard-Jones potential the Lennard-Jones/Spline potential obtains a continuous description of equilibrium and non-equilibrium properties by having a spline distance $r_s = (26/7)^{1/6}\sigma_{ij}$ and a spline potential[35]:

$$\begin{aligned} u_{ij} &= 4\epsilon_{ij}\left[\left(\frac{\sigma_{ij}}{r_{ij}}\right)^{12} - \left(\frac{\sigma_{ij}}{r_{ij}}\right)^{6}\right] && r \le r_s \\ u_{ij} &= \alpha_{ij}(r_{ij} - r_c)^3 + \beta_{ij}(r_{ij} - r_c)^2 && r_s \le r \le r_c \end{aligned} \tag{2.5}$$

Wherein α_{ij} and β_{ij} are defined as;

$$\alpha_{ij} = -\frac{387072}{61009}\frac{\epsilon_{ij}}{r_s^3} \qquad \beta_{ij} = -\frac{24192}{3211}\frac{\epsilon_{ij}}{r_s^2} \tag{2.6}$$

the cut off distance is set to be $r_c = (67/48)r_s$.

In NEMD, linear response theory is utilized to derive the transport coefficients. The molar flux for a component k in a layer ν can be computed as:

$$\mathbf{J}_{k,\nu} = \frac{\rho_{k,\nu}\mathbf{v}_{k,\nu}}{N_A} = \frac{N_{layers}}{VN_A}\sum_{i\in k, i\in layers}\mathbf{v}_i \tag{2.7}$$

Where N_{layers} is the number of layers in the system, $\mathbf{v}_{k,\nu}$ is the average velocity for a given layer and $\mathbf{v}_i$ is the velocity of a particle i. The temperature of each layer is computed from the average kinetic energy according to the equipartition principle:

$$\frac{3}{2}kT_\nu N_\nu = \frac{3}{2}kT_\nu \sum_{i\in layers} N_{k,\nu} = \frac{1}{2}\sum_{i\in layers} m_i\left|\mathbf{v}_i - \mathbf{v}_\nu\right|^2 \tag{2.8}$$

in which k is the boltzmann constant and m_i is the mass of particle i. The temperature in a shock wave will have different values in the x-, y- and z-direction and can be written as a tensorial quantity [30] i.e. the diagonal components can be written as:

$$T_{\nu,\alpha\alpha} = \frac{1}{(N_\nu - 1)k}\sum_{i\in\nu} m v_{i,\alpha}^2 \tag{2.9}$$

Here $v_{i,\alpha}$ is the velocity in direction α. The temperature in the shock direction is corrected to

$$T_{\nu,xx} = \frac{1}{(N_\nu - 1)k}\sum_{i\in\nu} m v_{i,\alpha}^2 - \frac{m}{k}v_\nu^2 \tag{2.10}$$

The pressure in a direction α is found by time averaging the microscopic pressure tensor.

$$p_{\nu,\alpha\beta} = \frac{N_{layers}}{V}\sum_{i\in layers}\left(m_i v_{v,\alpha}v_{i,\beta} + \sum_{i\neq j}\mathbf{F}_{ij,\alpha}r_{ij,\beta}\right) \tag{2.11}$$

Here $v_{i,\alpha}$ is the velocity of particle i in direction α, $\mathbf{F}_{ij,\alpha}$ is the force exerted on particle i from particle j in direction α, and $r_{ij,\beta}$ is the component of the vector from particle j to particle i in direction β. The overall pressure p can computed as the average over the diagonal pressure components i.e.

$$p_\nu = \frac{1}{3}(p_{\nu,xx} + p_{\nu,yy} + p_{\nu,zz}) \tag{2.12}$$

The measurable heat flux $\mathbf{J'}_{q,\nu}$ cannot be computed directly since it is not a mechanical property, it can however be computed with the total heat flux $\mathbf{J}_{q,\nu}$ where

$$\mathbf{J'}_{q,\nu} = \mathbf{J}_{q,\nu} - \sum_{i\in k} H_k\mathbf{J}_{k,\nu} \tag{2.13}$$

H_k is the partial molar enthalpy of a component k. The total heat flux can be computed in terms of mechanical properties in the form:

$$\mathbf{J}_{q,\nu} = \frac{N_{layers}}{V} \sum_{i \in layers} \left(\left[\frac{1}{2} m_i v_i^2 + \phi_i \right] \mathbf{v}_i + \frac{1}{2} \sum_{i \neq i} [v_i \cdot \mathbf{F}_{ij}] \mathbf{r}_{ij} \right) \tag{2.14}$$

Where ϕ_i is the potential energy of particle i in the field of all of the other particles, $\mathbf{F}_{ij}$ is the force acting on particle i due to j.

All these properties are computed in dimensionless numbers where the particle mass m, σ and ϵ are used as characteristic mass, length and energy. See Table A.1 in the Appendix for conversions. With the potential- and kinetic energy NEMD can compute the specific internal energy u and specific enthalpy h.

$$u_\nu^* = u_{pot,\nu}^* + \frac{3}{2} T_\nu^* \tag{2.15}$$

Where $u_{pot,\nu}^*$ is the dimensionless specific potential energy, which is computed for a layer ν by summing the potential energy of each particle ϕ_i and dividing by the amount of particles in the layer N_ν, the superscript * is the dimensionless version of a property. The specific enthalpy can then be computed using the internal energy, pressure and density

$$h_\nu^* = u_\nu^* + \frac{p_\nu^*}{\rho_\nu^*} \tag{2.16}$$

Note that specific energies are per particle and not per mole.

2.3 The Navier-Stokes equations

The theory behind the Navier-Stokes equations is presented, starting with a derivation of the pressure tensor, then a formulation of the equations, and lastly a short description of the Finite Volume method (FVM) and numerical stability. Note that we refer to the N-S equations as an extension of the Euler equations [14] with diffusive fluxes and not to the momentum equation, which is often called the Navier-Stokes equation.

2.3.1 The pressure tensor

The pressure tensor will play a role in both the modeling and the computation of the entropy production. In order to elaborate on the pressure tensor each term must be regarded in the correct dimensions as a tensor, vector or scalar contribution. The pressure tensor can be written as

$$P = p\delta + \Pi \tag{2.17}$$

Where p is the pressure scalar, δ is the Kronecker delta and Π is the viscous pressure tensor [36]. The viscous pressure tensor Π for a fluid is given as

$$\Pi = -\eta \left(\nabla \mathbf{v} + (\nabla \mathbf{v})^T - \frac{2}{3} (\nabla \cdot \mathbf{v}) I \right) - \zeta (\nabla \cdot \mathbf{v}) I \tag{2.18}$$

in which η is the shear viscosity, $(\nabla \mathbf{v})^T$ is the transpose of the velocity gradient, I is the identity matrix and ζ is the bulk viscosity. The velocity gradient can be expressed as a tensor in the form

$$\nabla \mathbf{v} = \begin{bmatrix} \frac{\partial \mathbf{v}_x}{\partial x} & \frac{\partial \mathbf{v}_x}{\partial y} & \frac{\partial \mathbf{v}_x}{\partial z} \\ \frac{\partial \mathbf{v}_y}{\partial x} & \frac{\partial \mathbf{v}_y}{\partial y} & \frac{\partial \mathbf{v}_y}{\partial z} \\ \frac{\partial \mathbf{v}_z}{\partial x} & \frac{\partial \mathbf{v}_z}{\partial y} & \frac{\partial \mathbf{v}_z}{\partial z} \end{bmatrix} \tag{2.19}$$

Writing out the viscous pressure tensor in tensor notation then yields

$$\Pi = -\eta \left(\begin{bmatrix} 2\frac{\partial \mathbf{v}_x}{\partial x} & \frac{\partial \mathbf{v}_y}{\partial x} + \frac{\partial \mathbf{v}_x}{\partial y} & \frac{\partial \mathbf{v}_z}{\partial x} + \frac{\partial \mathbf{v}_x}{\partial z} \\ \frac{\partial \mathbf{v}_y}{\partial x} + \frac{\partial \mathbf{v}_x}{\partial y} & 2\frac{\partial \mathbf{v}_y}{\partial y} & \frac{\partial \mathbf{v}_z}{\partial y} + \frac{\partial \mathbf{v}_y}{\partial z} \\ \frac{\partial \mathbf{v}_z}{\partial x} + \frac{\partial \mathbf{v}_x}{\partial z} & \frac{\partial \mathbf{v}_z}{\partial y} + \frac{\partial \mathbf{v}_y}{\partial z} & 2\frac{\partial \mathbf{v}_z}{\partial z} \end{bmatrix} - (\frac{2}{3} - \zeta) \left(\frac{\partial \mathbf{v}_x}{\partial x} + \frac{\partial \mathbf{v}_y}{\partial y} + \frac{\partial \mathbf{v}_z}{\partial z} \right) I \right) \tag{2.20}$$

Describing this in tensorial terms yields a symmetric viscous tensor. Note that the bulk viscosity is often low for a monoatomic fluids and have often been neglected, but work with shock waves have shown that the inclusion of the bulk viscosity more accurately described the shock front [37]. The second term only contributes to the diagonal and will not affect the symmetry. This gives an expression for the viscous stresses in the system.

As we will be studying a shock wave propagating in the x-direction we simplify the equation to one dimension, which yields a pressure tensor normal to the shock front that has the form:

$$P_{xx} = p - \left(\frac{4}{3}\eta + \zeta \right) \frac{\partial v}{\partial x} \tag{2.21}$$

2.3.2 The Navier-Stokes equations

The Navier-Stokes equations, stems from the conservation equations that describe the conservation of mass, momentum and energy. A general description of the equations can be written as

$$\frac{\partial(\rho\psi)}{\partial t} + \nabla(\rho \mathbf{v}\psi) + \nabla \cdot \mathbf{J} = S \tag{2.22}$$

where ψ is the conserved quantity like mass, momentum or energy and S is a source/sink term. The equation consists of three terms: accumulation in the system i.e. the transient term $\frac{\partial(\rho\psi)}{\partial t}$, transfer into and out of the system which are the convection $\nabla(\rho \mathbf{v}\psi)$ and flux term $\nabla \cdot \mathbf{J}$, and a source/sink term S where the quantity is either generated or lost e.g. a component lost or produced in a chemical reaction [38].

The conservation equations are quite intuitive and serve as good equations for mathematical modelling, though they can often require some dimensional simplifications to be less computationally demanding to model. In order to compare a modelled result to NEMD simulations, the system must remain compressible and transient. Since the shock travels in the axial direction, the x-dimension is warranted. By applying assumptions such as symmetry and that the average velocity remains unchanged in the $y-$ and z direction since the shock wave propagates in the axial direction, leads to the vectorized conservation equations on the form:

$$\frac{\partial Q}{\partial t} + \frac{\partial F(Q)}{\partial x} = S \tag{2.23}$$

where Q is a vector of the conserved variables density ρ, momentum ρv and total energy E[19].

$$Q = \begin{bmatrix} \rho \\ \rho v \\ E \end{bmatrix} \tag{2.24}$$

E is given as $E = \rho\left(u + \frac{v^2}{2}\right)$. The vector $F(Q)$ can be seen as the vector of fluxes for the system and can be written as

$$F(Q) = \begin{bmatrix} \rho v \\ \rho v^2 + p \\ v(E+p) \end{bmatrix} \tag{2.25}$$

Lastly there are the source terms, or the diffusive fluxes $S(Q)$, which consist of viscous and conductive contributions.

$$S(Q) = \begin{bmatrix} 0 \\ \frac{\partial}{\partial x}\left(\frac{4}{3}\eta\frac{\partial v}{\partial x}\right) \\ \frac{\partial}{\partial x}\left(\frac{4}{3}\eta v\frac{\partial v}{\partial x}\right) + \frac{\partial}{\partial x}\left(k\frac{\partial T}{\partial x}\right) \end{bmatrix} \tag{2.26}$$

Note that the bulk viscosity ζ is not included in the source term as it was not incorporated in the N-S equations.

This set of partial differential equations (PDEs) is too difficult to solve analytically, thus, we chose to apply a spatial discretization scheme and integrated in time using an ODE integrator.

2.3.3 The Finite Volume Method and numerical stability

For the numerical formulation we chose a Finite Volume Method (FVM) as an approximation of the integral conservation law. Starting from the one-dimensional scalar conservation equation, where the source term can be incorporated into the flux, yields

$$\frac{\partial Q}{\partial t} + \frac{\partial F(Q, \nabla Q)}{\partial x} = 0 \tag{2.27}$$

By integrating over the control volume $\Delta x = x_{i+\frac{1}{2}} - x_{i-\frac{1}{2}}$, see appendix A.1 for the derivation, yields the semi-numerical formulation:

$$\frac{\partial Q}{\partial t} = -\frac{F_{i+1/2} - F_{i-1/2}}{\Delta x} \tag{2.28}$$

To define the flux F we utilize the FORCE flux by Toro [19]. The FORCE flux is the arithmetic average of the Lax–Friedrichs flux and the two–step Lax–Wendroff flux and possesses several desirable qualities, it is unconditionally stable and does not require knowledge of the systems eigenvalues which in turn makes it ideal for a shock wave with a LJ/s fluid, but the flux is known to be quite dissipative, which could affect profiles [19, 39]. The flux is formulated in Chapter 3.

For the temporal integration, we will utilize an explicit Runge Kutta 5th order integrator. Explicit methods are often more time efficient [40], but are in turn less numerically

stable, which puts restrictions on the temporal and spatial grid size for the modelled phenomena. For the Navier-Stokes equations there are two restrictions, a convective- and a diffusive condition. The convective contribution is known as the Courant–Friedrichs–Lewy (CFL) condition and can be formulated as follows. The solution remains numerically stable given that:

$$\Delta t < CFL_{max} \cdot \frac{\Delta x}{\max_{k,\mathbf{n}=1} |\lambda_k|} \tag{2.29}$$

where CFL_{max} is the maximum CFL number, often given as $CFL = \frac{v\Delta t}{\Delta x}$ where v is the magnitude of the velocity, based on the integration method, Δt is the transient grid length $\Delta t = t_{i+1} - t_i$ and λ_k are the eigenvalues of the Jacobian of the inviscid fluxes [41]. The diffusive condition can be formulated as

$$\Delta t < \frac{\Delta x^2}{2D} \tag{2.30}$$

Where D is the diffusion coefficient [41]. Though this thesis won't contain a stability analysis, these conditions should be kept in mind as they put restrictions on choice of the temporal and spatial grid.

2.4 Excess properties

A way of determining the properties of a shock wave is to consider it as a surface. The shock front, similar to the interface between two phases, has sharp gradients between its adjacent bulk phases and is shallow in thickness. Using the assumption that thermodynamic relations between surface variables remain valid locally even when the system is overall out of equilibrium it becomes possible to treat the shock front as an autonomous thermodynamic system [42].

The properties of the shock wave, such as the surface temperature T^s, can thus be computed by determining the excess densities of the surface. Excess densities can be defined by choosing the position l of a dividing surface in the interfacial region and then extrapolate the bulk densities to the dividing surface. The integral over the difference between the actual density minus the extrapolated densities defines the excess densities:

$$\rho_i^s = \int_a^b \left[\rho_i - \rho_i^d \Theta(l-x) - \rho_i^u \Theta(x-l)\right] dx \tag{2.31}$$

Here a and b are positions in the adjacent bulk phases, Θ is the Heaviside function and the superscripts d and u are the extrapolated bulk densities downstream and upstream of the surface. A visualisation of this is shown in Figure 2.2.

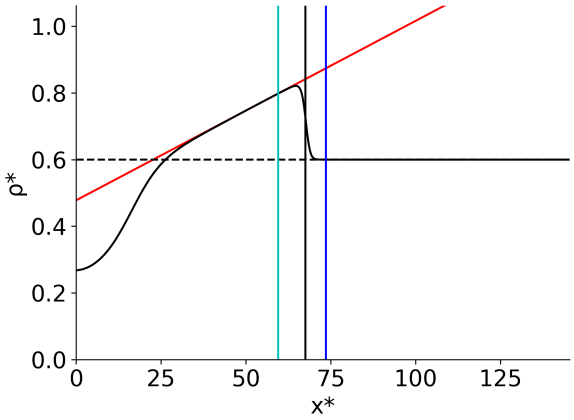

Figure 2.2: Visualisation used for determining the Gibbs equimolar surface. The dark dotted line is the extrapolated upstream bulk density and the red line is the extrapolated downstream bulk density. The cyan, black and blue axis lines are a, l and b respectively.

Before computing excess densities a choice of dividing surface l is needed. This can be the frequently used Gibbs equimolar surface or the surface of tension. The Gibbs equimolar surface is defined as a geometrical plane going through points in the interfacial region, similarly situated with conditions of adjacent matter. By definition, the surface l is found by requiring that the excess particle density is zero:

$$0 = \int_a^b \left[\rho - \rho^d \Theta(l - x) - \rho^u \Theta(x - l)\right] dx \tag{2.32}$$

Knowing the Gibbs equimolar surface enables us to determine the shock wave position, its velocity v^s and, if the the speed of sound is known, the Mach number at a given time. The velocity of the surface is given as:

$$v^s(t) = \frac{dl(t)}{dt} \tag{2.33}$$

The Gibbs equimolar surface also enables us to calculate excess densities such as the excess enthalpy ρ_h^s, internal energy ρ_u^s and entropy ρ_s^s. The excess enthalpy and internal energy density can be calculated directly from the NEMD using Eq. 2.31 while excess entropy has to be computed using an equation of state. With the excess internal energy and entropy we can determine the temperature of the surface T^s. Using the integrated form of the Gibbs equation for a surface [35] combined with the Gibbs-Duhem equation yields:

$$d\rho_u^s = T^s d\rho_s^s + \mu^s d\rho^s \tag{2.34}$$

where μ is the excess specific Gibbs energy. Given that the definition of the Gibbs equimolar surface is $\rho^s = 0$ the surface temperature can be written as:

$$T^s = \frac{d\rho_u^s}{d\rho_s^s} \tag{2.35}$$

2.5 Perturbation theory

The equation of state that will be utilized for shock wave modeling and calculating shock wave properties is a first order perturbation theory adapted for the Lennard-Jones/spline potential known as the uv-theory [31].

The main idea of perturbation theory, put simply, is to write the potential as a sum of two terms, the potential energy of the unperturbed system U_0 and the perturbation U_1 [43].

$$U = U_0 + U_1 \tag{2.36}$$

Here, U_0 represents a hard sphere potential while U_1 represents an attractive potential. It is then possible to write the residual Helmholtz free energy $a^{res} = A/(N_S kT)$ as a summation of n-th order of a terms on the form [31],

$$a^{res} = a_0 + \sum_{i=1}^{n} \Delta a_i^u \tag{2.37}$$

Here a_0 is the residual helholtz energy of the reference fluid of the intermolecular potential while Δa_i^u is i-th order perturbation contribution due to the perturbation potential.

The first order uv-Theory is based on the observation that a first order expansion of equation 2.37, when modified to recover the exact second-virial coefficient B_2, will bound the Helmholtz energy on the form:

$$\Delta a_1^v \equiv \Delta a_1^u + (\Delta B_2 - \Delta B_{12}^u)\rho \lessapprox a^{res} - a_0 \tag{2.38}$$

wherein $\Delta B_2 = B_2 - B_{20}$ is the total perturbation contribution to the second virial coefficient, B_{20} is second virial coefficient of the reference fluid and ΔB_{12} is the first order contribution to the second virial coefficient. The superscript 'v' indicates that the first order pertubation term Δa_i^u is modified by the second order virial expansion.

This lower bound can be connected together with the rigorous upper bound given by a first-order u-expansion which is the Gibbs Boguliubov inequality [44] thus yielding the inequality:

$$\Delta a_1^v \lessapprox a^{res} - a_0 \leq \Delta a_1^u \tag{2.39}$$

The uv-theory consists of interpolating the Helmholtz energy between these bounds, which gives

$$\begin{aligned} a^{res} - a_0 &= \Delta a_1^v \Delta + \phi^u(\Delta a_1^u - \Delta a_1^v) \\ &= \Delta a_1^v + (1 - \phi^u)(\Delta B_2 - \Delta B_{21})\rho \end{aligned} \tag{2.40}$$

Where the interpolation function $\phi^u(\rho, T) \leq 1$ is known as the "u-fraction".

The implementation of the uv-theory on the LJ/s fluid is then done in the following manner: The intermolecular potential is split into reference and perturbation term on the form

$$\begin{aligned} u_0(r) = u_{LJ/s}(r) - u_{LJ/s}(r_{split}) \qquad & r < r_{split} \\ u_0(r) = 0 \qquad & r \geq r_{split} \end{aligned} \tag{2.41}$$

Here u_0 is the reference part while the pertubation part is given as:

$$w(r) = u_{LJ/s}(r) - u_0(r) \tag{2.42}$$

The splitting radius r_{split} is the distance in which the LJ/s potential is at its minimum $r_{min} = 2^{(1/6)}\sigma$. In this Section, σ denotes the Lennard-Jones size parameter.

The Helmholtz energy of the reference fluid a_0 is determined using the first order Mayer-f expansion about the hard sphere fluid [44]:

$$a_0 = a_d^{HS} - 2\pi\rho \int_0^\infty y_d^{HS}(r)(e_0(r) - e_d^{HS}(r)r^2 dr \tag{2.43}$$

Starting within the integral, $y_d^{HS}(r) = g_d^{HS}(r)/e_d^{HS}(r)$ and $e_d^{HS}(r) = exp(-\beta u_d^{HS}(r))$ define the cavity-correlation function [45]. The hard sphere fluid diameter d is based on the Boltzman-factor criterion [46]:

$$d = \sigma \left(\frac{2}{1 + \sqrt{T^*}} \right)^{1/6} \tag{2.44}$$

, lastly the term a_d^{HS} is obtained using the Carnahan and Starling equation of state [47]:

$$a_d^{HS} = \frac{4\eta - 3\eta^2}{(1-\eta)^2} \tag{2.45}$$

where the packing fraction η was defined as $\eta = (\pi/6)\rho d^3$.

Moving to the perturbation terms, the first order perturbation term Δa_1^u can be defined in terms of the pair correlation function of the reference fluid

$$\Delta a_1^u = 2\pi\rho\beta \int_{d'}^\infty g_{d'}^{hs}(r) w(r) r^2 dr \tag{2.46}$$

Here, d' is the effective hard-sphere diameter calculated by nullifying the integral terms in equation 2.43 and $g_{d'}^{hs}$ is the pair-correlation of hard spheres. By numerically integrating over a grid of $0 < \rho^* < 1$ and $0.2 < T^* < 10$ yields empirical functions for Δa_1^u and ΔB_{21}^u, see [31] for the empirical equations of Δa_1^u, ΔB_{21}^u, B_2 and B_{20}.

With access to Δa_1^u, ΔB_{21}^u, B_2 and B_{20} we can compute Δa_1^v. This leaves the u-fraction ϕ^u left to derive in order to determine the residual Helmholtz energy. Molecular Dynamic simulations were used to determine ϕ^u based on the equation

$$\phi^u = \frac{a_{MD}^{res} - a_0 - \Delta a_1^v}{\Delta a_1^u - \Delta a_1^v} \tag{2.47}$$

where a_{MD}^{res} is the residual Helmholtz energy computed using MD simulations. With the results an ansatz function was proposed:

$$\phi^u = \tanh(c_1\rho^* + c_2\rho^{*c_3} + c_3\rho^{*c_5}) \tag{2.48}$$

wherein c_i denote correlated constants (see [31]).

With access to reference and perturbed variables the residual Helmholtz energy a^{res} can be computed using temperature and density. The helholtz energy will in turn, due to the fundamental thermodynamic relations, allow us to compute entropy, pressure, enthalpy and internal energy.

In the work by van Westen and coworkers the conclusion, regarding the uv-theory, was that the theory provided a promising alternative, proving to be more accurate than other perturbation theories [31]. However, there were still room left for improvement, especially concerning the determination of thermal properties such as the internal energy and heat capacity. This was specifically for temperatures within 10 percent of the critical temperature ($1 \leq \beta \leq 1.25$), where $\beta = \frac{\epsilon}{kT}$. This could be relevant for the implementation of the EOS in the N-S equations, since the perturbation theory will be utilized to determine temperature and pressure based on the internal energy.

2.6 Models for viscosity and thermal conductivity

Modelling a LJ/s fluid with the Navier-Stokes equations requires equations for the fluids transport properties, namely the shear viscosity η and thermal conductivity κ. The transport properties also need to remain accurate within the temperature and density range of the shock wave. In this work we have utilized a transport property model adapted for argon [48]. For the liquid phase, the transport equations were used due to their validity and robustness for a wide array of densities and temperatures [48], though they had not been compared to temperatures and densities as large as those which would be used to simulate a shock wave in this work.

The viscosity and conductivity are defined as the sum of a dilute (η^0,κ^0) term, dependent on temperature, and a residual term (η^r,κ^r), dependent on density and temperature. The expression for the viscosity can be written as:

$$\eta = \eta^0(T) + \eta^r(\tau, \delta) \tag{2.49}$$

in which $\tau = \frac{T_c}{T}$ and $\delta = \frac{\rho}{\rho_c}$ are dimensionless variables based on the critical enhancement of argon. The thermal conductivity is written in the same form, although it does include a critical enhancement term which has omitted in this work due to the value being computationally demanding.

The dilute terms uses Chapman-Enskog theory fitted to experimental data; the viscosity is written as

$$\eta^0 = \frac{0.0266958\sqrt{M_m T}}{\sigma_{Ar}\Omega(T^*)} \tag{2.50}$$

where Ω is the collision integral, σ_{Ar} is the Lennard-jones size parameter of argon, and M_m is the molar mass. The dilute viscosity is then used to derive the dilute conductivity:

$$\kappa^0(T) = N_1 \left[\frac{\eta^0(T)}{1\mu\text{Pa}\cdot\text{s}}\right] + N_2\tau^{t_2} + N_3\tau^{t_3} \tag{2.51}$$

In this equation N_i are coefficients of the collision integral and t_i are fitted exponents. The residual terms are empirical based equations and can be found, along with the coefficients, in the work of Lemmon and Jacobsen [48].

A model for the bulk viscosity ζ was considered for the NEMD data. Originally postulated to be zero [49], later work has found that the inclusion of the term leads to more physically sound solutions, including for complex phenomena such as shock waves where the inclusion of the bulk viscosity has led to a more accurate prediction of the shock wave location and strength [37].

Since a model for the bulk viscosity of a LJ/s fluid has yet to be derived, a bulk viscosity model for argon was used [50]. The model can be written as a function of density:

$$\zeta^* = \left(\frac{\rho}{\rho_c} - 1\right)^{\alpha_1} + \alpha_2 \tag{2.52}$$

Where the coefficients α_i depend on temperature:

$$\alpha_i = a_i + b_i \cdot \tanh\left(c_i\left(\frac{T}{T_c} - 1\right)\right) \tag{2.53}$$

Note that T_c and ρ_c are the critical temperature and density of argon, while a_i, b_i, and c_i are coefficients which can be found in the corresponding article [50]. It should also

be noted that the transport coefficient equation was in good agreement with experimental data, but were not compared to liquids with temperatures above the critical temperature. The transport coefficient equation was fitted with the condition $\zeta \geq 0$ to ensure the equation remained physically valid, following the 2nd law of thermodynamics.

2.7 Deriving the entropy production

By the excess entropy production we refer to the entropy production along the shock front, mathematically this can be formulated as integrating the local entropy production over the length of the front [30]:

$$\sigma_s^s = \int_a^b \sigma_s(x,t)dx \tag{2.54}$$

Where a and b are the same positions used to determine Gibbs equimolar surface and excess densities located before and after the shock wave.

We have utilized five methods to determine the excess entropy production. We present the equations used and their underlying assumptions. First we explain the local equilibrium assumption, then we review methods which use the local entropy production, methods that assume the shock front is a surface of discontinuity and lastly we present a method for approximating the excess entropy production in the half cell.

2.7.1 The local equilibrium assumption

Before reviewing the methods for determining the excess entropy production it is important to address the assumption of local equilibrium. The local equilibrium assumption is the assumption that the thermodynamic relations remain valid for a chosen volume element even though the overall system is not in equilibrium [35]. This assumption is integral to all the methods for determining excess entropy production, either as an assumption within the methods derivation or by the use of the EOS, which also assumes local equilibrium. Work by Hafskjold and coworkers have indicated that the shock front is not in local equilibrium [42], which makes the assumption an important factor to consider.

For the simulation methods the assumption is part of the N-S equations, as the EOS is used to compute temperature and pressure. The NEMD simulations only uses the EOS to determine entropy related properties. The methods for determining excess entropy production all have the assumption of local equilibrium, but the assumption is applied differently in the local methods compared to the surface methods. In the local method we assume local equilibrium in the shock front while in the surface methods we consider the shock front as an autonomous thermodynamic system with its own surface properties.

2.7.2 The Linear irreversible thermodynamic (LIT) method

A classical way of determining the local entropy production σ_s is the formulation by de Groot and Mazur named the Linear Irreversible Thermodynamic (LIT) method[51]:

$$\sigma_s = J_q' \frac{\partial}{\partial x}\left(\frac{1}{T}\right) - \frac{1}{T}\Pi_{xx}\frac{\partial v}{\partial x} \tag{2.55}$$

Here, the entropy production is due to a conductive and viscous contribution. The derivation of the equation involves two assumptions, the assumption of local equilibrium everywhere in the fluid and the Gibbs equation for bulk systems. Note that this is the only method where the entropy or entropy density is not directly given in the equations.

2.7.3 The bulk balance method (BBM)

The bulk balance method uses the entropy balance equation to compute the entropy production,

$$\sigma_s = \frac{\partial}{\partial t}\rho_s + \frac{\partial}{\partial x}J_s \tag{2.56}$$

Here, ρ_s denotes the entropy density while J_s is the entropy flux which is a combination of the heat conduction and entropy transported by fluid flow:

$$J_s = \frac{J_q'}{T} + \rho_s v \tag{2.57}$$

The BBM method consists of a transient- and spatial derivative. Unlike the LIT method, the BBM has no assumption of local equilibrium in the equation nor does it involve the Gibbs equation, but the BBM method does utilize the EOS to derive the entropy, which means that the method also assumes local equilibrium everywhere in the fluid.

2.7.4 The surface balance method (SBM)

In the surface balance method we use the assumtions made in the excess properties section 2.4 and combine it with the entropy balance (Eq. 2.56) to compute the excess entropy production:

$$\sigma_s^s = \frac{d\rho_s^s}{dt} + J_s^u(t) - v^s(t)\rho_s^u - J_s^d + v^s\rho_s^d \tag{2.58}$$

Here the superscripts u and d are the up- and downstream extrapolated properties on the surface for the entropy density and flux. The extrapolated properties are determined as the value of the property at the surface, which can be seen visualized in Figure 2.3.

Equation 2.58 yields the excess entropy production where the shock wave is considered a surface of discontinuity, but without using the Gibbs equation[30]. The SBM method, except for the transient derivative of the excess entropy density, only uses properties in local equilibrium outside the shock front, requiring up- and downstream extrapolations of the entropy flux and entropy density which are in the bulk phases, this makes the method more robust [30].

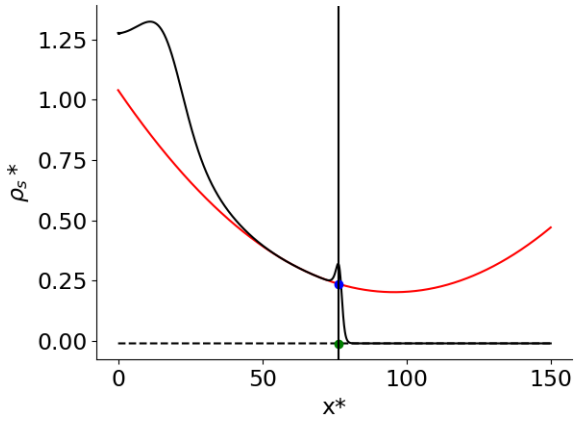

Figure 2.3: Visualisation used for determining the up- and downstream extrapolated properties. The green and blue dot are the extrapolated up- and downstream properties on the surface. The dark dotted line is the extrapolated upstream bulk density and the red line is the extrapolated downstream bulk density. The black axis line is the surface of discontinuity.

2.7.5 The Gibbs Excess method (GEM)

The Gibbs Excess Method (GEM) takes the SBM method a step further by using the Gibbs equation for a surface. The expression can be split as follows:

$$\sigma_s^s = [\sigma_q]_- + [\sigma_j]_- \tag{2.59}$$

The excess entropy production is a sum of the extrapolated local entropy production of the heat contribution $[\sigma_q]_- = \sigma_q^u - \sigma_q^d$ and mass contribution $[\sigma_j]_- = \sigma_j^u - \sigma_j^d$. The heat term is given as

$$\sigma_q = J_q' \left(\frac{1}{T} - \frac{1}{T_s} \right) \tag{2.60}$$

The mass term is set to be

$$\sigma_j = j \left(s - \frac{1}{T_s} \left[h + \frac{\Pi_{xx}}{\rho} + \frac{1}{2}(v - v^s)^2 \right] \right) \tag{2.61}$$

Where j is given as $j = \rho(v - v^s)$. The GEM method assumes the surface as a discontinuity and utilizes the Gibbs equation for a surface. This yields a method which gives detailed information about the energy dissipation in the shock front. For the derivation of the GEM method see Hafskjold et al. [30].

2.7.6 The Macro entropy method (MEM)

In addition the methods mentioned, we have developed a new method to calculate the entropy production based on knowledge of the volume element in the NEMD cell and the entropy balance (Eq. 2.56). The local entropy production in the cell can be written as:

$$\sigma_s = \frac{\partial \rho_s}{\partial t} + \frac{\partial J_s}{\partial x} \tag{2.62}$$

By integrating across the length of the cell L we compute the total entropy production of the NEMD cell as [35]:

$$\sigma_s^{cell,s} = \frac{\partial \left(\int_0^L \rho_s dx \right)}{\partial t} + (J_s^o - J_s^i) \tag{2.63}$$

Where J_s^o and J_s^i are the entropy flux into and out of the NEMD cell. Since there is no entropy flux into nor out of the cell we can eliminate the fluxes. Previous work showed that the entropy production of a shock wave is mainly located in the front, thus, the total entropy production will mainly consist of the excess entropy production of the shock wave i.e. $\sigma_s^{cell,s} \approx \sigma_s^s$. The excess entropy production can then be approximated as:

$$\sigma_s^s \approx \frac{\partial \left(\int_0^L \rho_s dx \right)}{\partial t} \tag{2.64}$$

The excess entropy production can then approximated by finding the time derivative of the integrated entropy density across the entire box. The method is similar to the BBM method, both using the entropy balance and the EOS to determine the excess entropy production.

Chapter 3

Simulating a shock wave with NEMD and the Navier-Stokes equations

3.1 Simulating a shock wave in NEMD

The NEMD simulations were carried out using an in-house Fortran code where the equations of motion were on the form:

$$\frac{\partial \mathbf{r}_i}{\partial t} = \frac{\mathbf{p}_i}{m_i} \tag{3.1a}$$

$$\frac{\partial \mathbf{p}_i}{\partial t} = \mathbf{F}_i(t) + \mathbf{R}_i(t) \tag{3.1b}$$

Wherein $\mathbf{r}_i$ and $\mathbf{p}_i$ are the position and momentum of particle i. $\mathbf{F}_i$ is the force acting on particle i from the other particles which can be written as [52]:

$$\mathbf{F}_{ij} = \frac{\partial u_{ij}}{\partial \mathbf{r}_i} \tag{3.2a}$$

$$\mathbf{F}_i = \sum_{j \neq i}^{N} \mathbf{F}_{ij} \tag{3.2b}$$

where u_{ij} is the LJ/s potential shown in equation 2.5. $\mathbf{R}_i$ is the required perturbation that is identified as the external force:

$$\mathbf{R}_i = (E_i - \overline{E})\mathbf{F}_i - \frac{1}{2}\sum_j \mathbf{F}_{ij}[\mathbf{r}_{ij} \cdot \mathbf{F}_i(t)] + \frac{1}{2N}\sum_{j,k} \mathbf{F}_{jk}[\mathbf{r}_{jk} \cdot \mathbf{F}_i(t)] \tag{3.3}$$

Here E_i is the kinetic and potential energy of particle i while $\overline{E}$ is the average energy of all the particles at time t. In boundary driven NEMD the perturbation is at the boundaries at the left and right hand side of the NEMD cell, see Figure 3.1, in the form of a velocity re-scaling.

The simulations consisted of 40 parallels with $N = 16000$ particles in a cell with a ratio of $L_x/L_y = 32$. The cell was split into 256 layers with a distance from each

other of $\Delta x^* = 1.176$. Each simulation consisted of three steps, first, an equilibrium simulation, second, the activation of the shock, and third, an NVE ensemble simulation of the shock wave travelling through the cell. At equilibrium the system had a density of $\rho^* = 0.6$ and temperature of $T^* = 2$. Using the equilibrium configuration, the shock was created by setting the total kinetic energy in two of the boundary layers to $5 \cdot 10^4$, this is equivalent to heating the layer to $T^*_{boundary} = 137.1$. With the configuration from step two, the shock was simulated. Each simulation ran for 10^5 steps consisting of a timestep of $t^* = 0.0002$ lasting a total of $t^*_{end} = 20$. Each equilibrium parallel was randomized with a Monte Carlo sequence, mixing up the position of the particles with m steps ranging from $m = 2.5 \cdot [1, 2, ...39, 40] \cdot 10^5$. The characteristic mass was the mass of an argon particle, the characteristic energy ϵ/k was $124K$, and the characteristic length was $\sigma = 3.418\mathring{A}$.

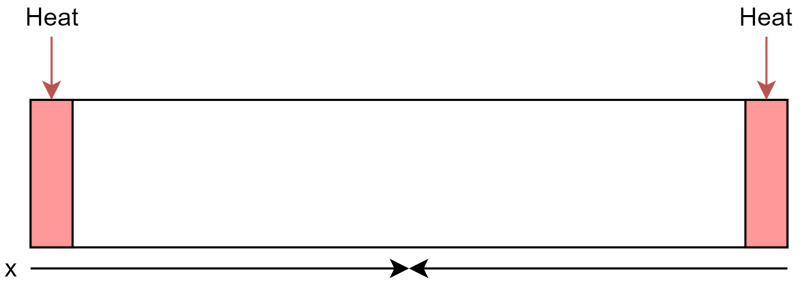

Figure 3.1: Illustration of the symmetric NEMD cell where the total kinetic energy are set in the boundary layers.

3.2 Simulating a shock wave with the Navier-Stokes equations

To simulate a shock wave similar to the NEMD simulations using the Navier-Stokes equation we had to set similar initial- and boundary conditions and have the same geometric proportions. With 256 layers of $\Delta x^* = 1.176$ and a ratio of $L_x/L_y = 32$ the total length and volume was derived as $L^* = 301.056$ and $V^* = 26736$. The initial conditions were set to be akin to the third step of the NEMD simulations when the boundary layers have just been heated. The initial density and velocity remained as they were in equilibrium i.e $\rho^* = 0.6$ and $v^* = 0$, while the internal energy $u^*(\rho^*, T^*)$ was computed with the EOS with a shock temperature T^*_H within the boundary layers L_m and a equilibrium temperature T^*_{eq} on the outside:

$$\begin{aligned} u^*(x^*, 0) &= u^*(\rho^*_{eq}, T^*_H) \qquad \frac{L^*}{2} - L^*_m < x^* < \frac{L^*}{2} + L^*_m \\ u^*(x^*, 0) &= u^*(\rho^*_{eq}, T^*_{eq}) \qquad \frac{L^*}{2} - L^*_m > x^*, x^* > \frac{L^*}{2} + L^*_m \end{aligned} \tag{3.4}$$

As the shock is induced in the middle of the cell the edges/boundaries of the cell were set to remain unchanged ($\frac{\partial Q}{\partial t} = 0$), another option would have been to set transmissive boundary conditions i.e $Q_{start} = Q_{end}$ like Titarev and Toro [53], but given that the shock wave was studied before it hit the boundaries keeping them unchanged seemed sensible.

The Navier-Stokes simulations were run for a duration of $t^* = 13.5$ with a spatial gridsize of $N_x = 4096$ and a transient grid of $K_t = 2161$.

3.2.1 Numerical formulation of the governing equations

The governing equations are discretized spatially with the FORCE flux, developed by Titarev and Toro [53]. The formulation is extended with a source term which is discretized with a finite difference method, and, instead of using explicit time differencing, we use an ODE integrator to integrate the transient differential.

The overall solution of the equations can be written on the form:

$$\frac{\partial Q_i}{\partial t} = -\frac{F_{i+1/2} - F_{i-1/2}}{\Delta x} + S(Q_i) \tag{3.5}$$

Where $F_{i+1/2}$ and $F_{i-1/2}$ are the FORCE fluxes on the right and left hand sides of the value i. The FORCE flux can be formulated as follows:

$$F^{FORCE} = \frac{1}{4}\left(F(Q_L) + 2F_M + F(Q_R) - \frac{\Delta x}{\Delta t}(Q_R - Q_L)\right) \tag{3.6}$$

Where the subscripts R and L are the left and right hand side of the interface position $1/2$. The flux F_M is the flux of the interface $F_M = F(Q^{1/2})$, the interfacial value $Q^{1/2}$ is calculated to be:

$$Q^{1/2} = \frac{1}{2}\left(Q_L + Q_R - \frac{\Delta x}{\Delta t}(F(Q_R) - F(Q_L))\right) \tag{3.7}$$

Moving to the formulation of the diffusive terms $S(Q)$, the main derivatives can be split in a similar manner to the main fluxes, as they are dependent on the interfacial values, while the internal derivative can be split using central differences, similar to the method named in the introduction of the work of Shen et al. [54].

$$\frac{\partial}{\partial x}\left(\mu\frac{\partial f}{\partial x}\right) = \frac{1}{\Delta x^2}\left(\mu_{i+1/2}(f_{i+1} - f_i) - \mu_{i-1/2}(f_i - f_{i-1})\right) \tag{3.8}$$

Here μ represents the transport coefficients $\mu = [\frac{4}{3}\eta, \frac{4}{3}v\eta, \kappa]$ and f the values of $[v, v, T]$ respectively.

3.2.2 Newtons method for determining temperature and pressure with the internal energy

The Navier-Stokes equations uses the equation of state to compute the pressure and temperature. The pressure is necessary to formulate the flux terms in the N-S equations and the temperature is needed to compute the viscous and conductive coefficients. The temperature and pressure are found by using the EOS in tandem with the Newton method [55].

Thermopack, the Python module which has access to the equation of state, has two functions `internal_energy_TV()` and `pressure_TV()`, which calculates internal energy and pressure, including their derivatives, based on temperature, volume and moles of particles as input. Since the aforementioned variables are given in the N-S equations, it is possible to determine the temperature by using the Newton method. There is only one unknown, the temperature, thus, only one root function is required:

$$f_1 = U(T, V_{in}, n_{in}) - U_{in} \tag{3.9}$$

here the variables with the subscript in are the given inlet values. As the temperature is the only non-constant, the derivative function can be written as

$$f_1' = \frac{\partial U(T, V_{in}, n_{in})}{\partial T} \tag{3.10}$$

With a temperature guess T_0 the approximate root of the function can be found using the recursive function

$$T_{n+1} = T_n - \frac{f_1(T_n)}{f_1'(T_n)} \tag{3.11}$$

wherein the recursion goes a limited number of times until the error margin $|T_{n+1} - T_n| < 1.48 \cdot 10^{-8}$ is met. The Newton function was implemented using the Python library Scipy [56] which has an effective Newton solver. The temperature guess for T_i was chosen as the value in the previous time step starting with the initial temperature, if the solution did not converge, the guess would revert to T_{eq}. With the computed temperature, pressure was computed with the `pressure_TV()` function. The Newton method was utilized not just for each index i, but also for the interfacial values $i + \frac{1}{2}$, acquiring $T_{i+\frac{1}{2}}$ and $P_{i+\frac{1}{2}}$ instead of computing them with the arithmetic average.

3.2.3 Integrating the system of Ordinary Differential Equations (ODEs)

With the spatial formulation of the N-S equations ready, the equations were evolved in time using an explicit 5th order Runge Kutte (RK5) integrator with the Scipy program `Solve_IVP()` [57, 56]. As input the ODE integrator takes the initial conditions of the conserved variables along with a vector of time points for which to solve the variables. The integrator would also take in a function detailing how the derivatives $\frac{\partial Q}{\partial t}$ were to be solved, which was where the FORCE flux, diffusive fluxes, and Newton method are formulated. The formulations were given in vector form using list comprehension in order to make the program faster. As output the function returns a matrix of the conserved variables for each step in the given vector of time points. For a full visualization of how the ODE integrator works with the spatial formulations see Figure 3.2.

3.3 Computing shock wave properties and the excess entropy production

Once the shock wave has been simulated with NEMD and the Navier-Stokes equations the data is processed separately before the simulation data are used to determine shock wave properties. The data from NEMD is processed with the program `annemd`, described in Appendix A.3, which computes temperature, density, pressure, fluxes and numerous other properties using the equations given in Section 2.2. The NEMD computation is done for each layer in the half cell at the times $t^* = [0.25, 0.75, 1.25....20]$. The program calculates these properties for each parallel which are then used to compute averages and errors, using the equations in Section A.4. Once the average values are attained the NEMD data is ready.

The N-S data has to go through a couple of processes before we can determine its shock wave properties. The output from the ODE integrator are vectors of the conserved variables $Q = [\rho, \rho v, E]$, these are reformulated to attain the density, velocity and internal energy which lets us compute temperature, pressure, viscosity and conductivity. The data is then converted to reduced units using Table A.1, and are saved for the same time steps

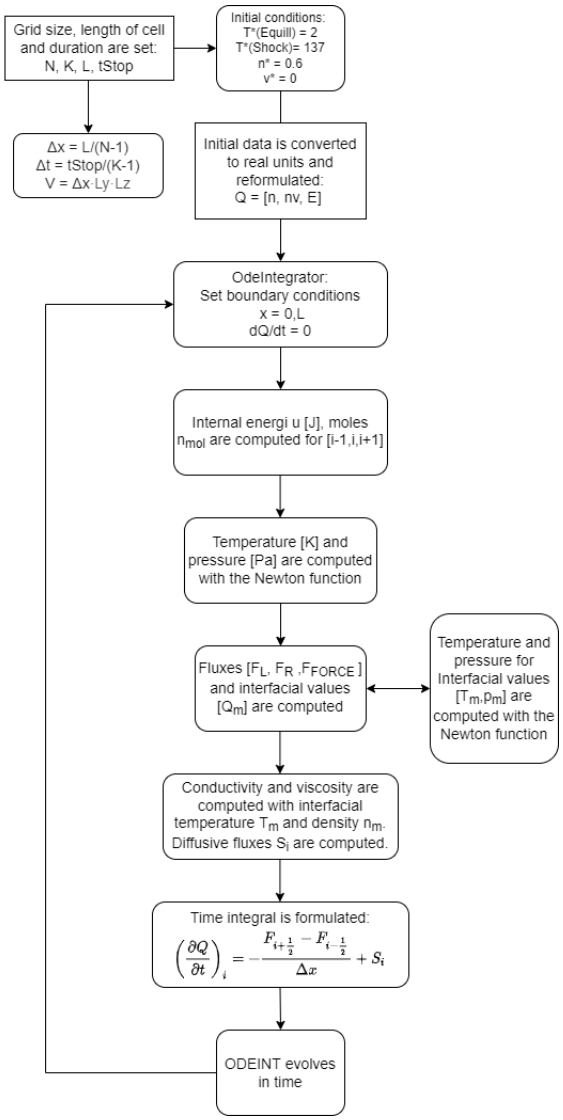

Figure 3.2: Flow sheet explaining the Python program written to solve the N-S equations.

t^* on the right hand cell ($x^* > L^*/2$). After this process the N-S data is ready for comparison. For a general description of the programs used see Appendix A.3.

3.3.1 Computing shock position, velocity, speed of sound and Mach number

The Gibbs equimolar surface was calculated for each time step with Equation 2.32 where a was set to be approximately a distance of $x^* = 5$, behind the middle value of the wave and b was set to be a distance of $x = 5$ in front. The integral of ρ was calculated using the Simpson method with the Python Scipy function `simps()`. The downstream extrapolated bulk densities were determined by making a linear regression of the densities from a to $a - 5$ while the upstream extrapolated densities were determined taking an average of the equilibrium values in front to get a zeroth order regression. The equation was solved for l using the Python Scipy function `root()` for the function:

$$0 = I_{simps} - \int_{a-5}^{l} (p_1^d x + p_0^d) dx - \int_{l}^{b} p_0^u dx \tag{3.12}$$

Where I_{simps} is the numerical integral of ρ from $a - 5$ to b, while p are polynomial coefficients. Note that the integration was done from $a - 5$ to ensure the density profile and the extrapolated downstream density were in contact. With the shock position at each time step we can determine the shock speed by plotting the shock position against time and fit it to a third degree polynomial. The shock speed is calculated as the derivative of the polynomial, or optionally using central differencing given that the data does not fluctuate. The speed of sound can be determined with the EOS in Thermopack with the function `speed_of_sound()` given that temperature, pressure and phase composition at equilibrium is known. With the shock speed and speed of sound available, the Mach number is determined using Equation 2.2.

3.3.2 Computing excess internal energy, entropy and surface temperature

Knowing the position of the shock front, the excess internal energy- and entropy density can be calculated. After attaining the specific internal energy using Equation 2.15, in the case of NEMD, we compute the specific entropy using the EOS. The EOS function `entropy_TV()` uses as input the temperature, volume and moles and returns the residual entropy s^*_{res}. After adding the ideal entropy contribution to the residual entropy the entropy was computed as:

$$s^* = s^*_{res} + \frac{3}{2} \ln T^* - \ln \rho^* \tag{3.13}$$

wherein the superscript '$*$' denotes that the units are in dimensionless form. The specific internal energy and entropy densities were computed as $\rho_u = \rho u$ and $\rho_s = \rho s$. With the entropy- and internal energy densities we can utilize the same procedure used to find the Gibbs equimolar surface to determine the excess density. Extrapolating over the same ranges and using the Simpson method to compute the density of the integral we instead use Equation 2.31:

$$\rho_i^s = I_{simps}^i - \int_{a-5}^{l} (p_{1,i}^d x + p_{0,i}^d) dx - \int_{l}^{b} p_{0,i}^u dx \tag{3.14}$$

the superscript i signifies the type of density property i.e. internal energy u or entropy s. With the excess densities the surface temperature can be determined using Equation 2.35. By plotting the excess internal energy density as a function of excess entropy density the derivative of the function will give the surface temperature. To fit function we chose a linear regression.

3.3.3 Determining excess entropy production with local methods and the MEM method

Knowing the surface properties, the excess entropy production can be calculated. We start with the local entropy production σ_s using the LIT and BBM methods. For both methods the procedure goes as follows, first the local entropy is computed for each point on the spatial grid, then the local entropy is numerically integrated over the shock front to yield the excess entropy production (Eq. 2.54). A simple method to solve the local equations can be done by computing the derivatives using fourth order finite differencing in the transient and spatial directions. For the BBM method is can be written as:

$$\sigma_s^{ij} = \frac{\rho_s^{i,j-2} - 8\rho_s^{i,j-1} + 8\rho_s^{i,j+1} - \rho_s^{i,j+2}}{12\Delta t} + \frac{J_s^{i-2,j} - 8J_s^{i-1,j} + 8J_s^{i+1,j} - J_s^{i+2,j}}{12\Delta x} \tag{3.15}$$

The superscripts i and j are the spatial and transient grid points respectively. The procedure was the same for the LIT method only using spatial derivatives. After computing the local entropy production in the cell, the excess entropy production is computed by numerically integrating (Simpson method) the local entropy production over the shock front, the shock front being the same range used to determine the equimolar surface and excess densities.

The MEM method procedure is similar to the determination of shock speed. Using Simpson integration, we integrate the entropy density over the entire half cell. Doing so for each time step we plot the integrated entropy density as a function of time and fit the plot with to a third order polynomial. The excess entropy production is then computed as the derivative of the polynomial using Eq. 2.64. This method can then be checked with the BBM method by integrating over the entire cell instead of the shock front.

3.3.4 Determining excess entropy production with surface balance methods

Determining the excess entropy production using the surface based methods requires upstream and downstream values. For the SBM method the extrapolated values are the entropy flux J_s and density ρ_s, while for the GEM method these are heat σ_q and mass σ_j terms. The upstream and downstream values are the value of the extrapolations at $x^* = l$, shown in Figure 2.3, by extrapolating the aforementioned variables, using the same ranges and polynomial orders used for determining the Gibbs equimolar surface and excess densities, the upstream and downstream values can be computed e.g. for the linear regression of the entropy flux we get $J_s^d = p_1^d l + p_0^d$.

There are some additional considerations. For the SBM method, we fit a linear regression to the excess entropy density to determine its transient derivative. For the GEM method the derivative in the viscous pressure tensor was approximated using a fourth order central difference scheme while, for the N-S equations, the enthalpy was computed with the EOS using the function `enthalpy()` in Thermopack.

Chapter 4

Results and Discussion

The following chapter consists of four sections. Section 4.1 discusses the overall thermodynamic properties of the NEMD- and N-S data and the subsequent shock wave properties. Section 4.2 concerns the entropy production, Section 4.3 will show comparisons between NEMD and the EOS, and Section 4.4 will delve into the methods used to determine the errors in NEMD.

4.1 General profiles and shock wave properties

In this section the results from the NEMD and N-S simulations are presented side-by-side starting with the general profiles of density, pressure, velocity and temperature in addition to the measurable heat flux. In the next subsection we compare the determination of the shock position and Mach number, and lastly we look at the determination of excess densities and surface temperature.

4.1.1 General profiles

Running the NEMD and N-S simulations, as described in the previous chapter, yielded the profiles shown in Figure 4.1 at time $t^* = 6.25$. This time step was chosen since the wave was evolved enough to compute shock wave properties and strong enough to show the characteristic differences between the simulation methods. Profiles for later steps were not included as they were not characteristically different. Starting with the NEMD data, Figure 4.1 has a sharp increase in temperature, density, pressure and fluid velocity which could indicate the presence of a shock wave. The profiles are relatively smooth, though not completely. The slight jaggedness of the profiles stem from NEMDs statistical nature which can be smoothed out by either increasing the number of particles [58] in the simulations or by averaging data with more parallels. Whether the slight jaggedness of the figures will affect subsequent extrapolations and calculations is difficult to tell, but instabilities in the data do not pair well with numerical methods such as central numerical derivatives, thus, the slight lack of smoothness could negatively affect the determination of the local entropy production down the road.

Moving to the N-S equations, we see the same increases in temperature, density, pressure and fluid velocity, with nearly identical trends to the NEMD simulations. Given that there are no fluctuations and that the profiles are similar to that of NEMD, we can assume

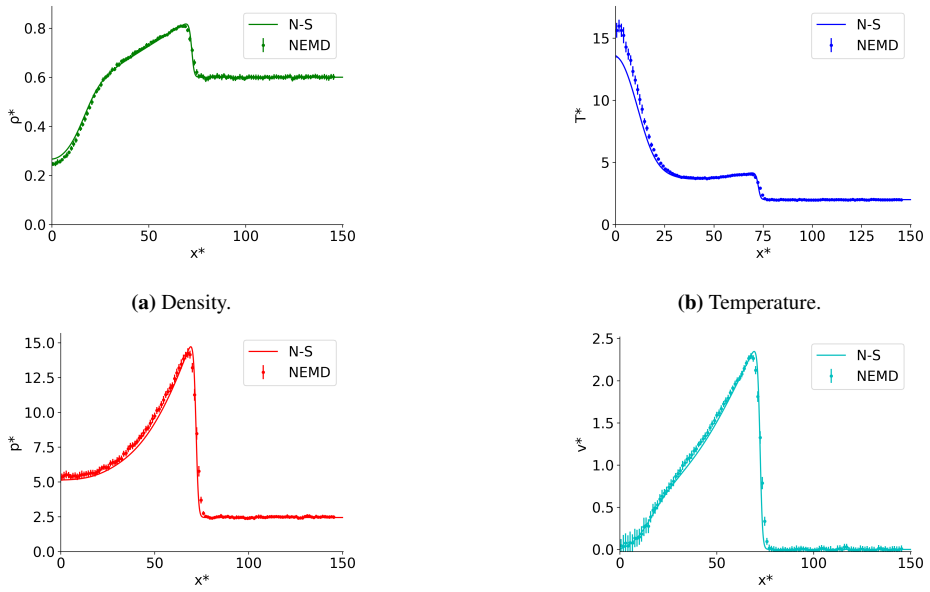

(a) Density.

(b) Temperature.

(c) Pressure.

(d) Velocity.

Figure 4.1: Averaged NEMD data and N-S data at $t^* = 6.25$ for density, temperature, pressure and fluid velocity. Uncertainties are three standard errors and were computed using data from the 40 NEMD parallels.

that the N-S equations satisfied the convective and diffusive restrictions on the transient- and spatial grid. There are some characteristic differences, as noted in the introduction, using the N-S equations would lead to sharper shock fronts, which can be seen replicated here in the density and pressure profiles. There could be another factor which has lead to a steeper front in the N-S equations, namely the transport coefficient equations. The N-S equations does not have a model for the bulk viscosity and has utilized an argon model for the thermal conductivity and shear viscosity, which given smaller coefficients could yield sharper profiles.

Since NEMD does not compute the shear viscosities explicitly we can only check the agreement between the methods respective measurable heat fluxes given in Figure 4.2. The measurable heat flux is within the error margin, with the exception of the shock front in which the NEMD values are larger. The sharper front could optionally or additionally be due to the less accurate transport coefficient equation and lack of viscous bulk contribution, which has been documented to more accurately describe the shock front (see Section 2.6).

Another difference between the methods (Figure 4.1) to note are the differences on the left hand side of the cell ($x^* < 20$), most notable for the temperature. This is likely due to the transport coefficient equations mentioned earlier, but it could be due to the FORCE flux's dissipative nature which could have the effect of dissipating the profiles, given the fineness of the grid and sharpness of the front it does not seem to affect the general profiles. The effect should not be disregarded though, as it could affect the excess entropy production down the line.

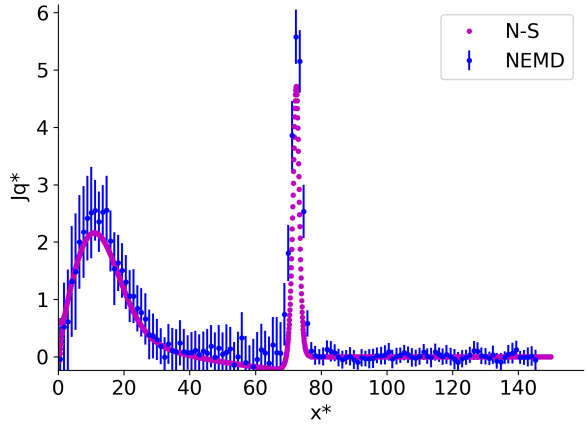

Figure 4.2: Averaged NEMD data and N-S data at $t^* = 6.25$ for the measurable heat flux. Uncertainties are three standard errors and were computed using data from the 40 NEMD parallels.

4.1.2 Shock Position and Mach number

With the densities we could determine the shock position using the definition of the Gibbs equimolar surface. The surface was determined in a nearly identical way, the extrapolation of the downstream density being a bit further behind the shock front by a distance of ca $\Delta x^* = 3$ for the N-S equations. Looking at Figure 4.3 the steepness of the front in the N-S equations does not lead to a characteristically different position of the surface, the surfaces being hard to tell apart.

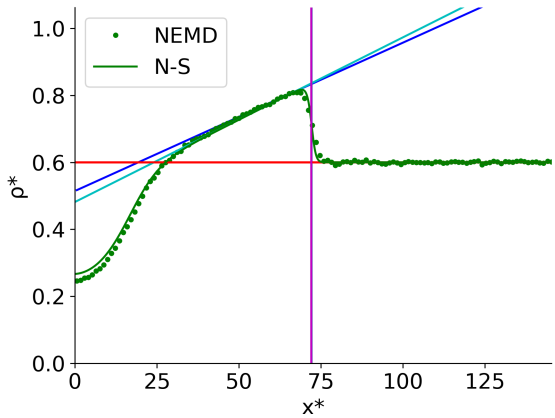

Figure 4.3: The method used for determining Gibbs Equimolar surface at $t^* = 6.25$. The dark and light blue line are the extrapolated bulk downstream densities while the magenta and yellow axis lines are the surface of discontinuity for the NEMD- and N-S methods respectively. The red line is the extrapolated upstream bulk density.

Looking at Figure 4.4, the two methods have similar surface positions, even the third order polynomials are hard to tell apart. The similarity is due to the definition of the equimolar surface which is not affected by the sharpness of the shock front. One could

expect the NEMD shock to be slightly slower as there are more viscous and conductive contributions.

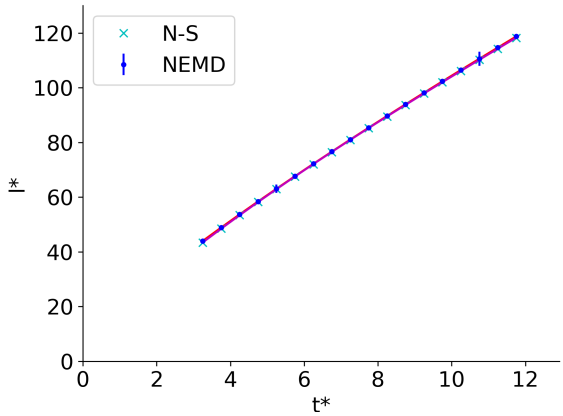

Figure 4.4: The NEMD and N-S shock wave positions as a functions of time fitted with a third order polynomial. The red and magenta polynomials are fitted to the NEMD- and N-S simulations respectively. Uncertainties are three standard errors and were computed using data from the 40 NEMD parallels.

With the fitted polynomials, we determined the shock speed and, by using the equilibrium data as input for the EOS, computed the speed of sound to be $v^*_{sound} = 4.7$. With these properties we determined the Mach number of the shock wave at each point in time, as seen in Figure 4.5. The sharp gradients are indeed shock waves, in both methods, as they are travelling at supersonic speeds. Interestingly, the N-S wave seems to travel slower than the NEMD wave, but given that the N-S method is within the margin of error the small differences could be due to inaccuracies in the polynomial fit.

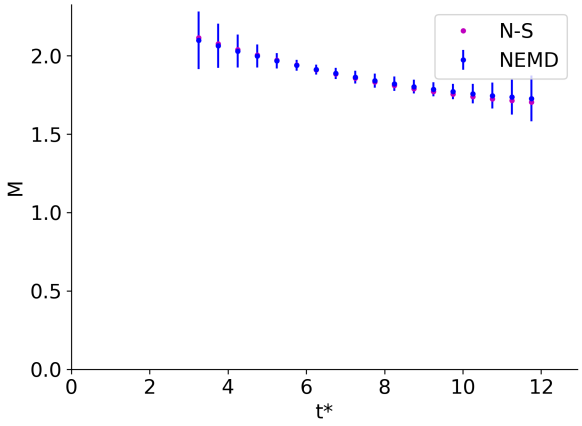

Figure 4.5: Mach numbers, computed using Eq. 2.2, for the N-S and NEMD data at a given time. Uncertainties are three standard errors and were computed using data from the 40 NEMD parallels.

Overall, the agreement between the methods seem promising for determining the subsequent shock properties. A point of discussion which has been reserved for Section 4.4

is the accuracy of error bars for the shock position, Mach number and effects of averaging NEMD parallels on the shock front.

4.1.3 Excess densities and surface temperature

To determine the excess internal energy- and entropy density we extrapolated their respective densities using the same ranges that were used for determining the Gibbs equimolar surface i.e. $a - 5$ to a for the downstream properties and equilibrium properties for the upstream properties. Starting with the internal energy density, as seen in Figure 4.6, the stable downstream bulk data seem to be accurately described by a linear regression in both methods. The extrapolations proved less accurate at early stages due to the closeness to the creation of the shock making the downstream extrapolated difficult to describe with a linear regression.

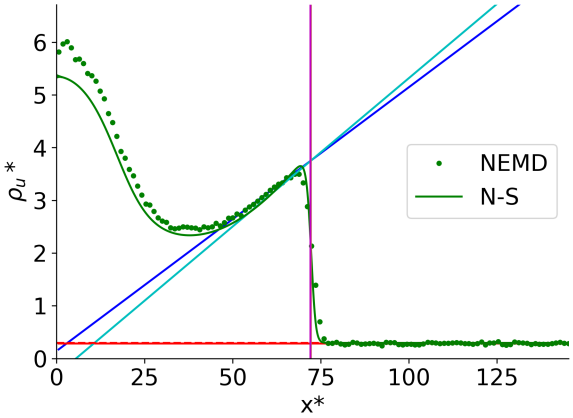

Figure 4.6: The method used for determining excess internal energy density at $t^* = 6.25$. The dark and light blue line is the extrapolated bulk downstream density while the magenta and yellow axis lines are the surface of discontinuity for the NEMD and N-S methods respectively. The red line is the extrapolated upstream bulk density.

Moving to the excess internal energy density (Figure 4.7) the NEMD data fluctuates some whereas the N-S data remains stable and within the error bars. Given that there are only fluctuations in the NEMD data indicate that the instability is likely statistical in nature, meaning that the extrapolations in NEMD might be less accurate.

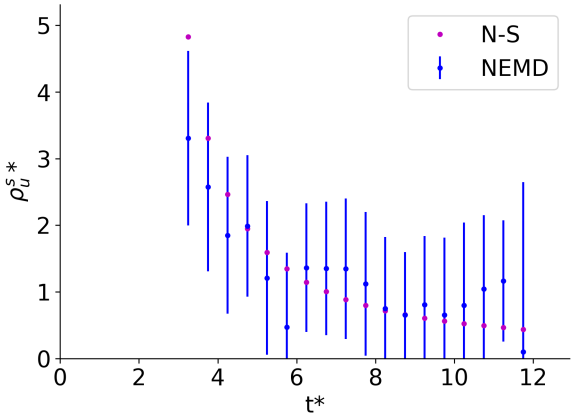

Figure 4.7: Excess internal energy density for the NEMD and N-S methods plotted against time. Uncertainties are three standard errors and were computed using data from the 40 NEMD parallels.

Moving to the extrapolations of the entropy density, shown in Figure 4.8, the extrapolation captures the downstream bulk accurately for both methodologies, though the NEMD data are a bit unsmooth. Note that the entropy was determined using the EOS, thus, making the NEMD data less independent as a method, as it uses the same tool as the N-S equations to determine a property. The EOS accuracy for determining NEMD properties will be the topic of discussion in Section 4.3.

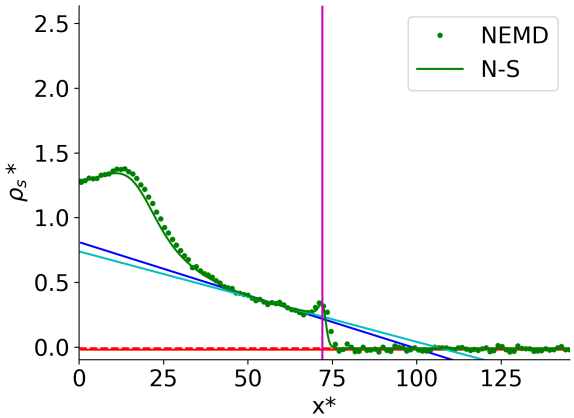

Figure 4.8: The method used for determining excess entropy density at $t^* = 6.25$. The dark and light blue line is the extrapolated bulk downstream density while the magenta and yellow axis lines are the surface of discontinuity for the NEMD and N-S methods respectively. The red line is the extrapolated upstream bulk density.

In Figure 4.9 there is a characteristic difference between the two methods, the excess entropy density being lower for the N-S equations. The difference could be due to several factors; the N-S equations has a transport coefficient equation for argon instead of an equation for the LJ/s fluid and a sharper shock front, but the difference could also be due to the use of the EOS for the NEMD data, a topic expanded upon in Section 4.3.

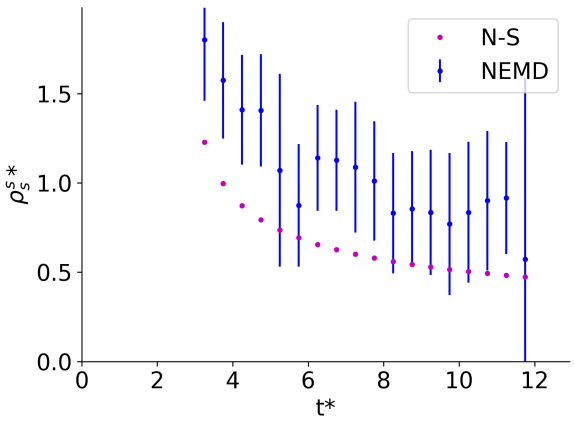

Figure 4.9: Excess entropy density for the NEMD and N-S methods plotted against time. Uncertainties are three standard errors and were computed using data from the 40 NEMD parallels.

The surface temperatures were determined by fitting a linear regression, as done in Figure 2.35, to the excess densities. The surface temperature for the NEMD shock was determined to be $T^{s*}_{NEMD} = 2.82 \pm 0.184$ and the N-S equations yielded a surface temperature of $T^{s*}_{N-S} = 3.20$. Both methodologies fulfill the criteria of being larger than the equilibrium temperature ($T_{eq} = 2$) and lower than the temperature post-shock temperature ($T^*_{ps} \approx 4.2$) i.e. $T^*_{eq} < T^{s*} < T^*_{ps}$, which was the case for gases in previous NEMD simulations [30]. That the N-S equations has a larger surface temperature should be due to the methods sharper gradients and transport coefficient equations, in the equations this showed in the form of the N-S equations lower excess entropy density. Note that both of the methods have assumed local equilibrium in the shock front, by utilizing the EOS, to compute the surface temperature.

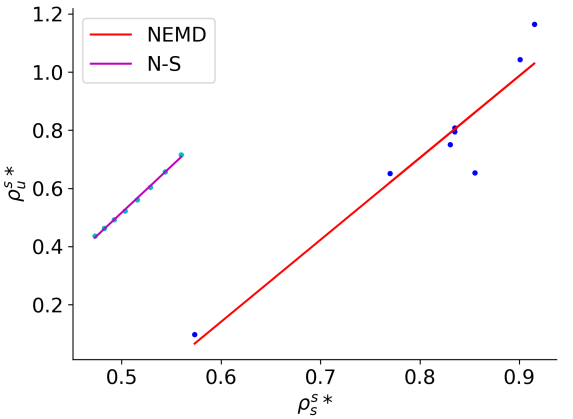

Figure 4.10: Excess internal energy plotted against excess entropy with a linear regression to determine surface temperature T^{s*} which was calculated to be $T^{s*}_{NEMD} = 2.82$ in the NEMD simulations and $T^{s*}_{N-S} = 3.20$ for the N-S equations.

4.2 The excess entropy production

With the general data and shock wave properties acquired, we can delve into the excess entropy productions. The structure will be similar to the Section 4.1, presenting the NEMD and N-S methodologies side-by-side, but we will expand upon this by comparing different entropy methods when necessary. We start with the local LIT and BBM methods, then the MEM method is reviewed before we focus on the surface methods SBM and GEM. Lastly we review the methods in the NEMD simulations and the N-S equations separately.

4.2.1 The BBM and LIT methods

With the LIT and BBM methods we can compute the local entropy production, which has the benefit of showing whether the method satisfies the 2nd law of thermodynamics i.e. $\sigma_s > 0$. Starting with the BBM method used with NEMD data, see Figure 4.11, it is clear the BBM method does not accurately describe the shock front, dipping below zero and oscillating before and after the shock. The LIT method remains strictly positive using NEMD data. The N-S data used a finer spatial and temporal grid and yielded strictly positive local entropy production. The BBM methods faults, in the NEMD calculations, can be pinpointed to the use of central differencing, a problem which arose in the work of Haskjold and coworkers as well. Possible ways of improving the BBM method were tested, such as fitting the NEMD results with spline system and normal distribution, but the data proved too unstable to improve the results significantly. The best option would have been to run larger simulations that would have yielded smoother profiles which, in turn, would be easier to apply numerical derivatives to.

Moving to the LIT method, the results remained strictly positive, which it should by definition. For the NEMD data we had to use the transport coefficient equations detailed in Section 2.6 to compute the shear- and bulk viscosities, seeing as the N-S equations had a lower excess entropy density we expect the transport coefficient equations to underestimate the viscous contributions, but to investigate this we need to compute the excess entropy density.

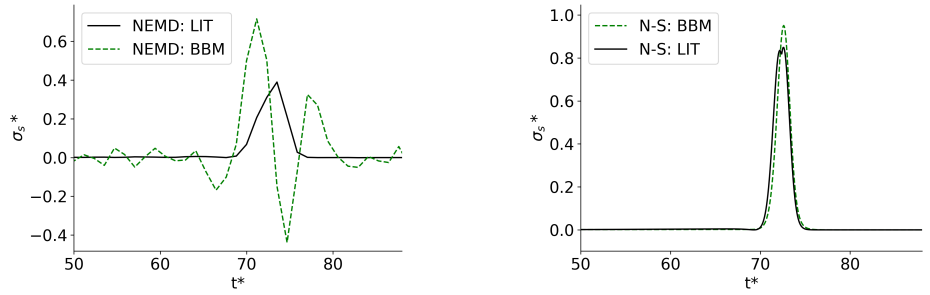

(a) NEMD. **(b)** N-S.

Figure 4.11: Local entropy production computed with NEMD- and N-S data using the LIT and BBM methods plotted against the length of the cell at time $t^* = 6.25$.

The excess entropy density can be seen in Figure 4.12 which raises a point which needs to be addressed, namely that the N-S equations compute a higher excess entropy production than the NEMD simulations with the LIT method. The main reason for this should be the use of the transport functions of argon explained in the previous paragraph, but it could also be caused by the N-S sharper gradients and its use of a finer grid, which

computes more accurate derivatives, a problem highlighted in the BBM method used on the NEMD data.

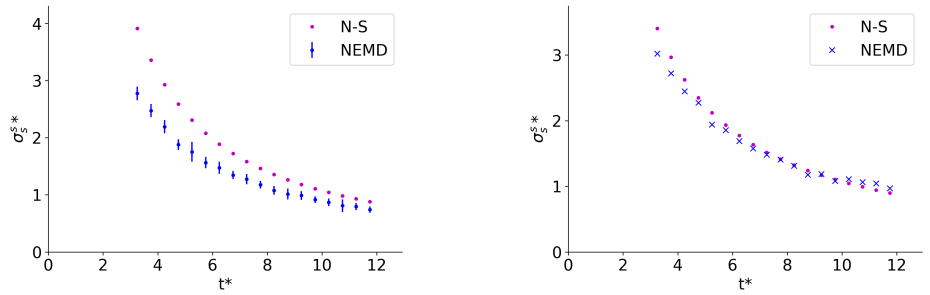

(a) LIT. **(b)** BBM.

Figure 4.12: Excess entropy production computed for the NEMD and N-S methods using the LIT and BBM methods. Uncertainties in the Subfigure 4.12a are three standard errors and were computed using data from the 40 NEMD parallels.

Turning to the excess entropy production with the BBM method, the oscillations in the local entropy makes the NEMD simulations excess entropy production highly questionable, but the method has proved fruitful for the N-S data which had a good agreement with the LIT method, though the BBM method had slightly larger values.

4.2.2 The MEM method

Integrating entropy density over the half cell we fitted the result to a third order polynomial, as shown in 4.13. The polynomials describe the profiles well and given that the integrated entropy density of NEMD is larger than the N-S equations seems sensible as we expect there to be more diffusive fluxes in NEMD.

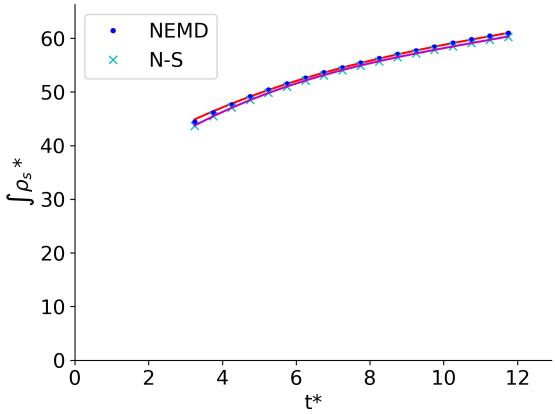

Figure 4.13: The integrated entropy density for the NEMD and N-S methods as a function of time fitted with a third degree polynomial.

Analyzing Figure 4.14 the NEMD and N-S methods have very similar results, the N-S equations remaining within the error bars. Given that the excess entropy production is for

the entire cell, the larger production in the N-S equations could be due to the dissipative nature of the FORCE flux. Looking at the profiles of temperature, the N-S data seems to have dissipated faster than the NEMD data while having a lower measurable heat flux, which could indicate that the N-S equations in fact are quite dissipative.

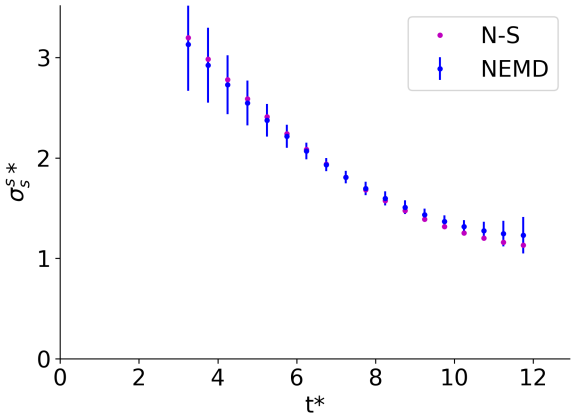

Figure 4.14: Excess entropy production plotted against time using the MEM method on the NEMD and N-S methodologies. Uncertainties are three standard errors and were computed using data from the 40 NEMD parallels.

The reliability of the MEM method was checked by using the BBM method integrated over the entire cell, in which data from the N-S equations was utilized due to its finer grid. The results can be seen in 4.15 where the BBM method shows good agreement with the MEM method. The figures should by definition be nearly identical since both methods were derived using the entropy balance, thus the difference arises from the use of different numerical methods, the MEM method fitted with a third order polynomial and the BBM method used central differencing. The slight kink, can likely be fixed by using a finer grid and central differences in the MEM method instead of fitting a polynomial, but the polynomial was chosen to keep the methods used on the NEMD and N-S data similar.

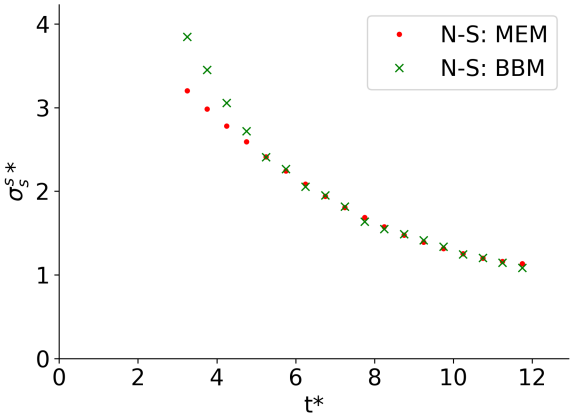

Figure 4.15: Excess entropy production plotted against time using the MEM method and BBM method integrated over the half cell on the N-S data.

4.2.3 The SBM method

With the excess entropy density, shock position and speed, we determined the excess entropy production using the Surface Balance Method (SBM). The transient derivative of the excess entropy density was found by fitting a linear regression to the latter part ($t^* > 8$) of the profile in Figure 4.9. For the NEMD and N-S methods the downstream properties were extrapolated with a first and second order polynomial respectively, the second order extrapolation fitted better with the N-S data which can be seen in Figure 4.16.

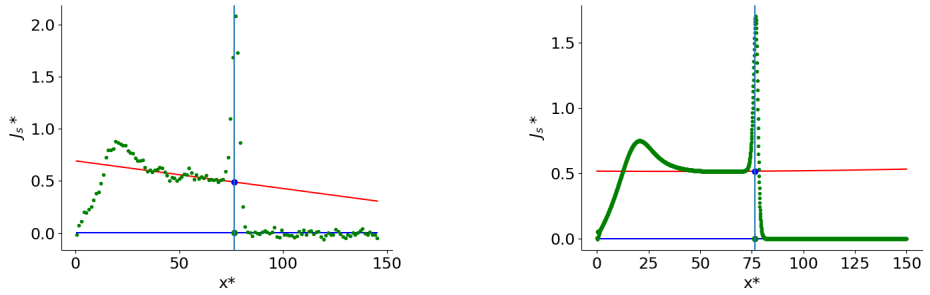

(a) NEMD.

(b) N-S.

Figure 4.16: The method used to determine the upstream- and downstream entropy flux at $t^* = 6.25$. The red line is the downstream extrapolated bulk, the blue axis line is the surface of discontinuity. The red line is the extrapolated upstream bulk density.

The excess entropy production can be seen in Figure 4.17 where the N-S equations remains within the error bars of the NEMD simulations. That the excess entropy production has the same magnitude in the two methods, which was the case using the MEM method, points to the presence of numerical viscosity in the N-S equations which will be elaborated upon in Subsection 4.2.5. The NEMD results fluctuate which, by checking the Fig. 4.16 is caused by the extrapolations of the downstream properties. Note that values

before $t^* > 8$ should be regarded as less accurate as the excess entropy density is given as a linear regression, but values before $t^* > 8$ are characteristically non-linear, see Figure 4.9.

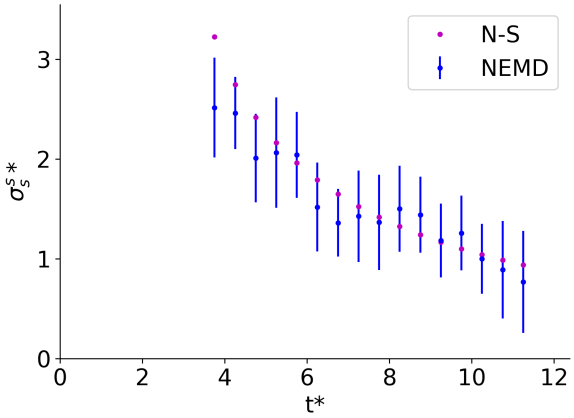

Figure 4.17: Excess entropy production plotted against time using the SBM method on the NEMD and N-S methodologies. Uncertainties are three standard errors and were computed using data from the 40 NEMD parallels.

4.2.4 The GEM method

Lastly, the Gibbs Excess Methods (GEM) will be investigated here. The entropy properties σ_q and σ_j had to be extrapolated to the surface to compute the excess entropy production. Checking the extrapolations σ_j, seen in Figure 4.18, we see the same characteristics from previous extrapolations where the N-S data seems more stable. The extrapolations of σ_q can be found in the Appendix (Fig. A.1) as it was found, similar to previous work, that it contributed little to the excess entropy production.

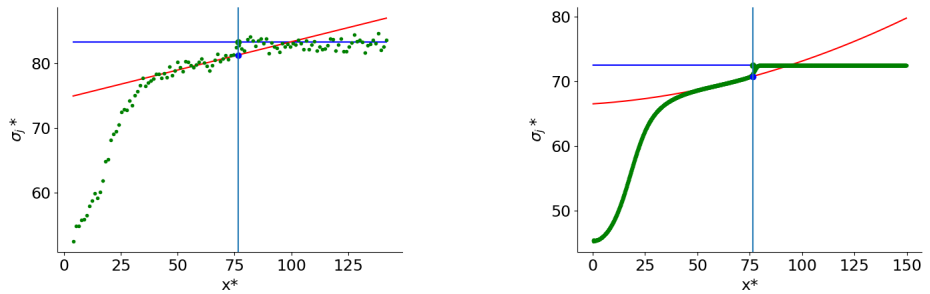

(a) NEMD.

(b) N-S.

Figure 4.18: The method used to determine the upstream- and downstream σ_j at $t^* = 6.25$. The red line is the upstream extrapolated bulk, the blue axis line is the surface of discontinuity. The red line is the extrapolated downstream bulk density.

Looking at the excess entropy production in Figure 4.19 we first have to address the large error bars, the large gaps are caused by computing the entropy production for each

parallel, wherein the data is less stable. With the N-S method yielding more stable results makes it clear that the fluctuations in the NEMD data are not caused by the implementation of the equations, but rather the statistical nature of NEMD. The GEM results raises the issue whether the NEMD system size has been too small with 16 000 particles, a subject we will return to in Section 4.4.

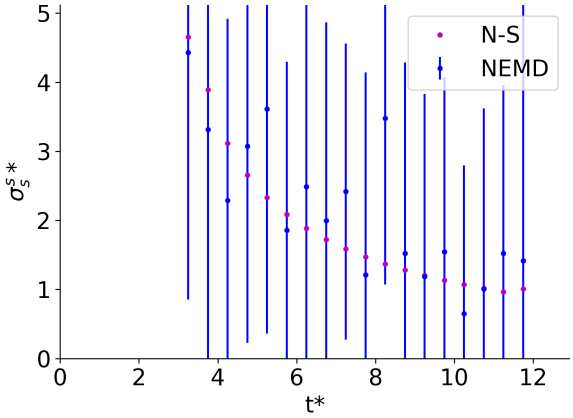

Figure 4.19: Excess entropy production plotted against time using the GEM method on the NEMD and N-S methodologies. Uncertainties are three standard errors and were computed using data from the 40 NEMD parallels.

4.2.5 Agreement between the Entropy methods

Having acquired the excess entropy production with five different methods we can investigate the overall agreement between these methods as well as characteristics of the methodologies. Starting with the N-S equations, shown in Figure 4.20 for $t^* > 8$ where the shock wave has stabilized, all the techniques share a similar profile. The MEM method stands out slightly by having a larger production, which was expected, seeing as the method computes the total entropy production of the cell.

Looking at the other methods they follow a similar pattern, the LIT and BBM method have the lower values, followed by the SBM method, while the GEM method computes the second highest excess entropy production, remaining under the MEM estimates.

The agreement between the LIT method and the other methods is an important matter to consider, as the LIT method is the only method which does not to use the EOS function for entropy. Given the similar profiles between the BBM and LIT method, it is safe to assume that the EOS entropy function computes accurate entropies at local equilibrium.

There is a noticeable difference between the local methods and the surface methods. This is likely due to equilibrium assumption where the LIT and BBM methods contain the assumption of local equilibrium in the front values whereas in the SBM and GEM methods considers the surface as its own thermodynamic system. Using surface properties in equilibrium for the shock front might compute a larger excess entropy production, even when the system used i.e. the N-S equations, has the assumption of local equilibrium. The slight difference might also caused by the use of second order extrapolations for the SBM- and GEM methods when we utilized N-S data.

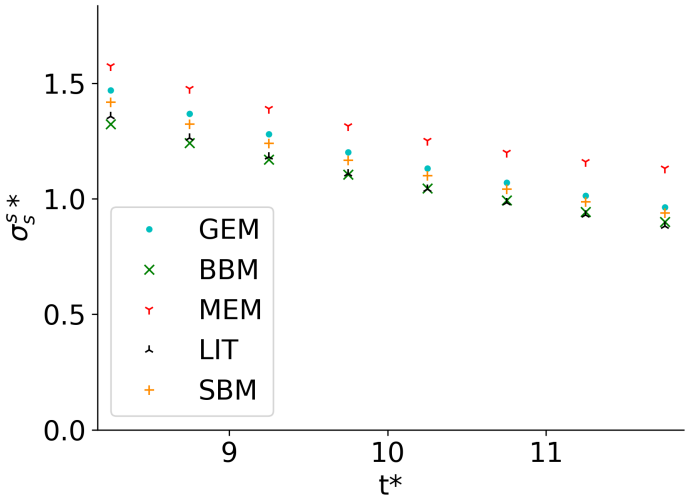

Figure 4.20: Excess entropy production plotted against time for the N-S equations using five different methods.

Considering the agreement of the methods with the NEMD simulations (Figure 4.21) yields similar results, the MEM method is the largest while the LIT method is the lowest. The more reliable methods proved to be the MEM, SBM and LIT methods, remaining relatively stable by computing excess entropy production which fluctuated little. BBM and GEM methods were less reliable; BBM, by having ”negative” local entropy production, and the GEM method, by computing highly fluctuating results.

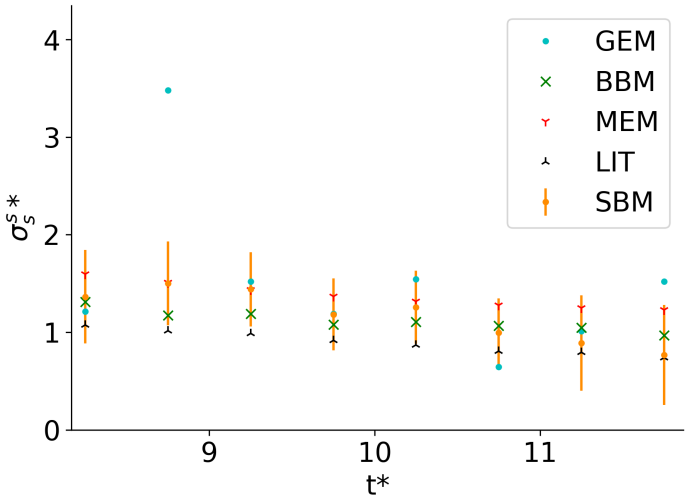

Figure 4.21: Excess entropy production plotted against time for the NEMD simulations using different methods. Uncertainties are three standard errors and were computed using data from the 40 NEMD parallels using the SBM method.

The LIT methods agreement with the other methods, in NEMD, is notably lower compared to those in the N-S equations. It could simply be due to the use of the transport coefficient equations of argon to determine the shear and bulk viscosity, but the use of central differences and the effects of averaging the NEMD parallels (discussed in Section 4.4) could make the derivatives in the LIT equation less steep.

4.2.6 Comparing the excess entropy production for the simulation methods

Lastly, we address the very similar entropy production of the NEMD simulations and N-S equations. From Figure 4.20 and 4.21 the excess entropy production is roughly the same throughout, with the N-S data remaining within the error bars for the MEM method. As mentioned in previous sections, the expectation was that the NEMD simulations would have a larger entropy production, since it has a viscous bulk contribution and a larger measurable heat flux, shown in Figure 4.2.

Starting with factors that could increase the excess entropy production using the N-S equation, we have the dissipative FORCE flux, the sharper shock front, the EOS, the assumption of local equilibrium, the implementation of the diffusive fluxes, and the use of a one dimensional model.

Given that the initial conditions are discontinuous, with a large temperature gradient, it was expected to be some numerical dissipation in the model. This seems to be the case given the lower temperature in the N-S profiles at the boundary layer compared to NEMD, which given the N-S lower conductivity and viscosity coefficients should have been higher. To quantify the numerical viscosity in a shock wave is difficult to check, especially given the presence of diffusive fluxes. An option to investigate this would have been to simulate a continuous heat gradient for an inviscid fluid and utilize the EOS entropy function to compute the entropy production, which using the LIT equation should have been zero. This would not give any information to how the FORCE flux works combined with the diffusive fluxes, but it could have offered information as to how the dissipative nature of FORCE affects the entropy production at a similar time- and length scale.

As noted in Section 4.1 the N-S profiles are slightly steeper in the front, which has been the case in previous studies. This does in turn lead to steeper gradients in the LIT and BBM methods which could contribute to the larger entropy production in the local methods. The sharper front also yielded different extrapolated values e.g. the difference in profiles for the entropy flux (Fig. 4.16), which could have increased the entropy production in the SBM and GEM methods.

The simplification to a one dimensional spatial grid was done due to computational efficiency, but it does limit the movement of the shock wave to the axial direction, whereas the particles in NEMD can move in three dimensions. This might have sharpened the front of the N-S method, but to check if this was the case, we would have had model the N-S equation in three dimensions.

The implementation of the diffusive fluxes could have affected the entropy production. As the FORCE flux is originally designed for the Euler equations the addition of the diffusive flux was done by applying central differences to the inner derivatives. The method has been utilized before, but with other central methods like the WENO scheme instead of the FORCE flux. Toro [19] noted that source contributions could be added by splitting the partial differential equations, first evolving the inviscid equations and then evolve the equation with the source contribution. Using the RK5 integration we evolved the entire equation instead of splitting it. Looking at the general profiles (Fig 4.1) and

measurable heat flux (Fig. 4.2), the integration described the shock wave well, but given that the formulation only uses central differences, it could have been slightly inaccurate when describing the diffusive fluxes which could have resulted in a higher entropy production.

The FORCE flux and the N-S equations steeper shock front are possible contributors to the larger excess entropy production, but there is still the use of the EOS and the assumption of local equilibrium. The assumption of local equilibrium is integral to the N-S equations and the entropy derivations since we have used the EOS. Meaning that even though the NEMD simulations does not assume local equilibrium, we still utilize the EOS to compute the excess entropy production in both the methodologies. We cannot say whether the assumption of local equilibrium leads to a lower excess entropy production, but we can compare other properties in NEMD and the EOS to get an impression of the accuracy in the shock front. The accuracy of the EOS and statistical nature of NEMD will be explored in the following sections.

4.3 Agreement between NEMD and the Equation of state

The EOS is utilized extensively with both the N-S equations and NEMD for determining shock wave properties. It plays an integral part in the N-S equations, determining temperature and pressure, and it gives access to the entropy, which enables us to compute the excess entropy production using the BBM, MEM, SBM and GEM methods. To ensure that the EOS is reliable and accurate within the ranges of temperature and density we compare properties which can be obtained in both methods, namely the pressure, internal energy and enthalpy. All comparisons were done at $t^* = 6.5$ similar to comparisons in previous sections.

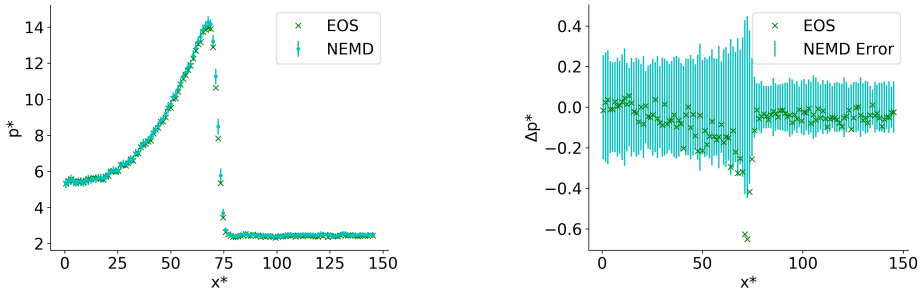

(a) Pressure.

(b) Pressure difference.

Figure 4.22: Comparison between NEMD pressure data and the EOS for a shock wave generated in NEMD. The EOS was given NEMD data for temperature, volume and moles of particles as input. The difference Δp is given as $\Delta p^* = p^*_{EOS} - p^*_{NEMD}$. Uncertainties are three standard errors and were computed using data from the 40 NEMD parallels.

Using NEMD data for temperature and density as input for the EOS, we check the difference across the shock wave between the EOS and NEMD. Starting with pressure, see Figure 4.22, the EOS is within the error bars with the notable exception of the shock front where the EOS computes a lower pressure. The difference could be due to the EOS assumption of local equilibrium, which is not the case for the temperature at the shock front. The perturbation theory is given an average of the temperature component and assumes temperature is still isotropic, this seems to result in a lower calculated pressure compared

to NEMD. There might be other explanations for the difference in the front though, like surface effects, the effect of the pressure component or perhaps the parameterization. To investigate this further would require a deeper dive into the perturbation theory derivations and comparisons to NEMD simulations.

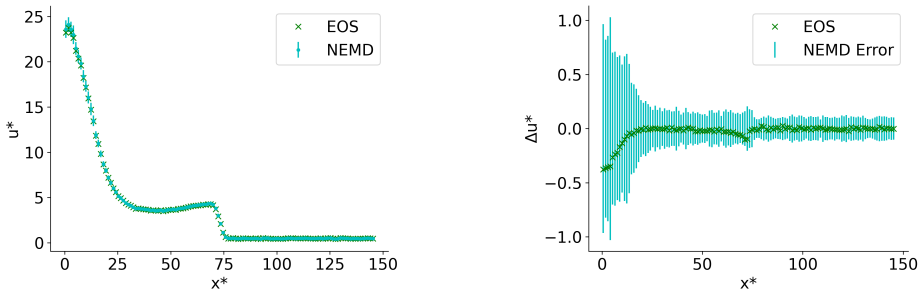

(a) Internal energy.

(b) Internal energy difference.

Figure 4.23: Comparison between NEMD internal energy data and the EOS for a shock wave generated in NEMD. The EOS was given NEMD data for temperature, volume and moles of particles as input. The difference Δu^* is given as $\Delta p^* = u^*_{EOS} - u^*_{NEMD}$. Uncertainties are three standard errors and were computed using data from the 40 NEMD parallels.

Much like the pressures, the internal energies, seen in Figure 4.23, are in good agreement with each other. They share the same trends, the EOS being lower in the shock front. The EOS An interesting point is that the EOS computes a lower internal energy closer to the boundary layer. This opens the possibility of the lower temperatures in the boundary layer of the N-S equations being due to the accuracy of the EOS, instead of numerical dissipation caused by the FORCE flux. The EOS had room for improvement in regards to the internal energy close to the critical region, since the initial temperature was above that region it does not seem to have affected the internal energies before and after the shock.

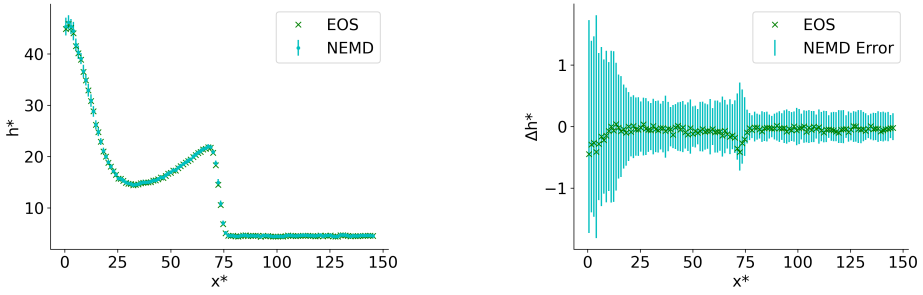

(a) Enthalpy.

(b) Enthalpy difference.

Figure 4.24: Comparison between NEMD enthalpy data and the EOS for a shock wave generated in NEMD. The EOS was given NEMD data for temperature, pressure and phase as input. The difference Δp^* is given as $\Delta h^* = h^*_{EOS} - h^*_{NEMD}$. Uncertainties are three standard errors and were computed using data from the 40 NEMD parallels.

The enthalpies (Figure 4.24) share trends with both the pressure and internal energy, having the largest difference at the shock front and differing some at the starting layers.

Overall the EOS captures the trend of the shock quite well with the exception of the

shock front. In the front, the EOS calculates lower values likely due to its assumption of local equilibrium. Given that EOS computes different values in the shock front it will likely affect its determination of entropy too, affecting the accuracy of the calculated surface temperature, as well as the BBM, MEM and the SBM method, as the SBM method utilizes the excess entropy density derivative.

4.4 Error analysis

40 NEMD simulations were used to determine the properties of a shock wave in NEMD. The average values of the parallels were used to determine surface properties while the error bars were determined computing properties for each parallel. The use of the average values and individual parallels both have their setbacks which could affect calculations and the accuracy of the NEMD data.

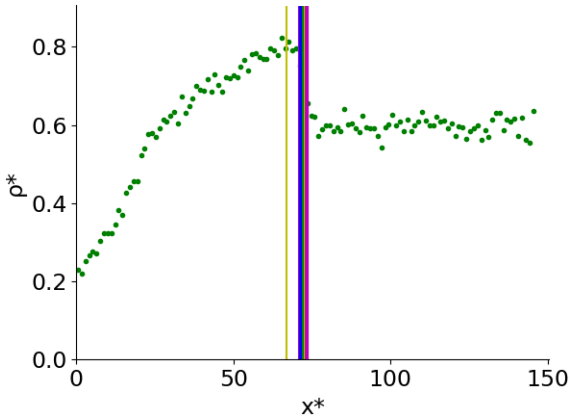

Figure 4.25: Density of the tenth parallel plotted against cell length at time $t^* = 6.25$. The multiple colored axis lines are the Gibbs equimolar surface for 40 NEMD parallels.

Starting with the use of an average of the simulations, averaging 40 parallels could have the effect of evening out the shock front, looking at Figure 4.25 and 4.26, the shock position is not identical for all simulations. The shock position does however remain between the equilibrium and maximum density for most parallels. Thus, computing an average could have the effect of dissipating the front by making the max value of the density slightly lower as the top differs in position. This could be one of the causes for the NEMD simulations yielding lower excess entropy productions, as the representation of the shock front consists of 40 shocks with slightly different positions.

Figure 4.26 and 4.27 serves to illustrate an issue with the determination of error bars. The methods used to determine shock wave properties and excess entropy production all require a non-fluctuating set of data in order to make accurate extrapolations, numerical derivations or integrals. In Figure 4.26 we see the consequence of utilizing fluctuating data, where the numerical procedure is not able to compute the shock position accurately in several parallels. This was the reason for the large error bars in the GEM method calculations (Fig. 4.19).

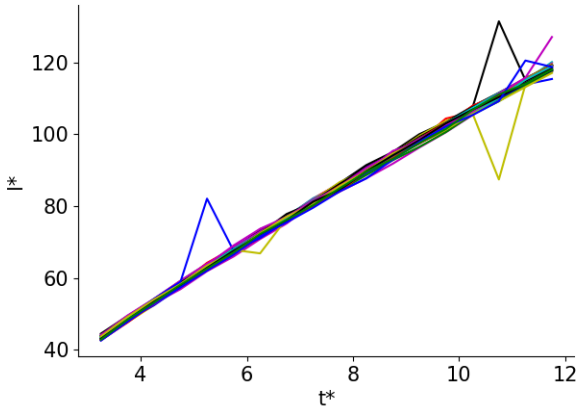

Figure 4.26: Shock position of the 40 NEMD parallels in multiple colors.

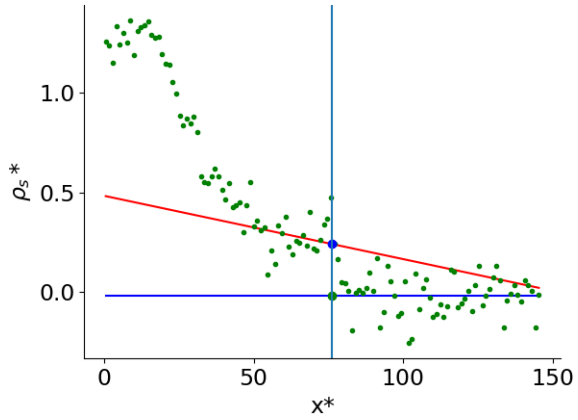

Figure 4.27: Method used to determine up- and downstream entropy density on the surface on of the tenth NEMD parallel at time $t = 6.25$.

In retrospect, the NEMD simulations would have benefited from using fewer parallels consisting of larger systems i.e. more particles. The increase in the number of particles would lead to less fluctuations since the statistical error of a particle property is inversely proportional to square number of particles $\sqrt{N}$ [58]. Thus, the increase in particles would have smoothed out the profiles and made methods for determining shock wave properties and excess entropy production more reliable as fluctuations would not affect extrapolations and numerical procedures to a significant degree. Sufficiently large simulations would also have made the determination of error bars more reliable, making extrapolations and numerical procedures less disordered for each parallel. Overall the system was large enough to determine properties such as the shock position, speed, surface temperature and excess entropy production using the MEM, SBM and LIT methods. To get more accurate uncertainties and utilize the GEM and BBM method would require larger simulations.

Chapter 5

Conclusion and future work

5.1 Conclusion

In this thesis we have simulated a liquid shock wave using NEMD simulations, developed by Hafskjold, and with the Navier-Stokes (N-S) equations. The implementation of the N-S equations combined an EOS for the LJ/s fluid, a transport coefficient equation for argon, the spatial FORCE flux, and an ODE integrator to solve a transient shock. The NEMD simulations and N-S equations both yielded similar profiles, but there were a couple of characteristic differences. The N-S equations had a sharper shock front, a lower measurable heat flux and a lower temperature in the boundary layer. The sharper front has been a characteristic of the N-S equations in previous work, while the lower heat flux was due to the use of argon transport coefficient equations. The lower temperature in the boundary, where the shock was generated, was likely due to a combination of the dissipative nature of the FORCE flux and the use of the EOS, which would compute lower internal energies at the boundary (see Fig. 4.23).

With the methodologies yielding similar profiles we calculated the shock wave properties using similar techniques. To determine the shock position and Mach number we used the definition of the Gibbs equimolar surface. Using the EOS, the speed of sound was determined to be $v^*_{sound} = 4.7$. By fitting the shock position to a polynomial we found the speed and subsequent Mach number. Both of the methods had a Mach number around 2, classifying them as supersonic shock waves. The shock wave, generated with the N-S equations, slowed down a bit faster compared to the NEMD simulations, but given that it remained within the error bars, the difference could be due to the the fitting of the third order polynomial to the NEMD data.

Having found the surface of discontinuity we determined the excess internal energy- and entropy densities and surface temperatures. The methodologies shared a similar profile for the excess internal energy density where the N-S data remained within the error bars. The excess entropy density was different for the two methods, sharing a similar profile, but the N-S data was lower and outside the error bars of NEMD. As a result the surface temperature of the N-S equations was higher i.e. $T^{s*}_{N-S} = 3.2$, which was not within the range of the NEMD temperature $T^{s*}_{NEMD} = 2.82 \pm 0.184$, but it still satisfied the criterion of being larger than the equilibrium temperature and lower than the temperature behind the shock. The difference in the models could be due the N-S equations sharper front and transport coefficient equations, but given that the EOS undervalued properties within the shock front it could also be the case for the entropy density.

With the computed shock wave properties we determined the excess entropy production. Starting with the local methods, the LIT method proved stable with both methodologies, giving larger values for the N-S equations because of its sharper front, use of transport coefficients, and the use of numerical derivatives. The BBM method did not work well with NEMD, giving negative local entropy production because of its coarser grid and inaccurate derivatives. The method did satisfy the second law of thermodynamics when it was used for the N-S equations.

The newly developed MEM method worked well with both of the simulation methods, deriving the excess entropy production for the entire half cell, the methods yielded very similar productions where the N-S data remained within the margins of NEMD. The MEM method also showed good agreement with the BBM method, though there were slight deviation because of the numerical techniques. We then moved to the surface methods SBM and GEM, where the SBM method worked with both methodologies, whereas the extrapolations for the GEM method were too unstable in NEMD.

At the time we suspected that the N-S equations yielded a similar excess entropy production because of the dissipative nature of the flux, but other factors could have contributed to the excess higher entropy productions, such as the sharpness of the shock front, assumption of one dimension, the use of the EOS, the assumption of local equilibrium and NEMD statistics, which we investigated further. The EOS was found to compute lower pressure, internal energy and enthalphy in the shock front of the NEMD simulations. Checking the error analysis, the NEMD system was found to be too small to reliably determine certain properties, namely the excess entropy using the BBM and GEM method. Computing the shock position for each parallel also showed that the shock position would differ slightly which could have affected the sharpness of the NEMD shock front.

Overall, the NEMD and N-S methods have successfully simulated a liquid shock wave, NEMD using the Newton's equations of motion whereas the N-S equations used the conservation of mass, momentum and energy with diffusive fluxes. Both methods managed to calculate shock wave properties such as the shock position, Mach number and surface temperature, wherein the N-S equations had a higher surface temperature. All of the excess entropy production methods worked with the N-S equations yielding similar results. For NEMD the system proved too small to utilize the BBM and GEM methods, whereas the MEM, SBM and LIT methods yielded more stable results. Though the EOS had slight issues in the shock front, it was in good agreement with NEMD across the range of the shock wave remaining within the uncertainties.

5.2 Future work

There are a lot of avenues to the study of shock waves utilizing the two methodologies we can explore. The most immediate work would be to improve upon the NEMD implementation by running larger simulations with more particles, and then run N-S simulations at similar initial conditions. We can use the methods for computing the entropy production to investigate the dissipative FORCE flux further by modeling the inviscid Euler equations, and we could study the perturbation theory in further detail by checking the theory's agreement with NEMD in equilibrium at higher temperatures, which could enable us to model stronger shocks.

Regarding new applications, a good start would be to investigate whether the N-S method works for gases. Given that the work by Hafskjold and coworkers were done studying shock waves in gases, their work is readily available for comparison. In this work we used an argon transport coefficient equation, but there are low-density transport

coefficients equations available for the LJ/s fluid [59]. These low-density transport coefficients equations can be implemented in the N-S method and used to simulate a shock wave at the same initial conditions as the NEMD simulations done on gases.

There are numerous amounts of techniques to discretize the spatial and temporal grid in the N-S method, thus, to explore different schemes can benefit the methods accuracy and speed. For the spatial grid we can test the weighted essentially non-oscillatory (WENO) scheme which is widely used and has a higher order accuracy than FORCE. For the ODE integrator the function `Solve_IVP()` can easily utilize several other methods such as a 8. order RK integrator, the `LSODA` method which automatically switches between implicit and explicit solvers, and an implicit Runge Kutta method. There is also methods outside the `Solve_IVP()` function which can be combined with the spatial grid. Note that we only utilized the RK5 method in this work due to its speed.

The numerical formulation of the N-S equations could be improved upon by analyzing the diffusive fluxes. In our work we used central differences, but formulations can be expanded to a higher order which has been done for other models such as the WENO scheme [54]. The inclusion of bulk viscosity should improve the accuracy of the method further, as it has done so in previous work [37]. There is not transport equations for the bulk viscosity for the LJ/s fluid as of this moment, but it could be developed in future work.

The N-S method could be used to model other liquids. Given an accurate EOS and transport coefficient equations for the given fluid, we can utilize the same discretizations to model a shock wave in the new fluid. Given access to the entropy and other properties we can then compute the excess entropy production of that fluid. Possibly the most interesting liquid to model would be water, given its abundance and relevance in fields such as medicine.

Bibliography

[1] E. Mach and P. Salcher. Photographische fixierung der durch projektile in der luft eingeleiten vorgange. *Annalen der Physik*, Vol. 286(10):277–291, 1887.

[2] J. D. Andersen. *Fundamentals of Aerodynamics*. McGraw-Hill Education, 6th edition, 2017.

[3] M. Thiel, M. Nieswand, and M. Dörffel. The use of shock waves in medicine - a tool of the modern or: an overview of basic physical principles, history and research. *Minimally Invasive Therapy Allied Technologies*, Vol. 9(3-4):247–253, 2000.

[4] R. B. Anoop, K. K. Jyothish, and A. A. Arjun. A review on applications of shock wave. *International Research Journal of Engineering and Technology (IRJET)*, Vol. 6(4):4367–4370, 2003.

[5] H. Reichenbach. Contributions of Ernst Mach to fluid mechanics. *Annual Review of Fluid Mechanics*, Vol. 15:1–28, 1983.

[6] W. J. M. Rankine. XV. on the thermodynamic theory of waves of finite longitudinal disturbance. *Philosophical Transactions of the Royal Society A*, Vol. 160:277–288, 1870.

[7] H. Hugoniot. Memoir on the propagation of movements in bodies, especially in perfect gases (first part). *Journal de l'École polytechnique*, Vol. 57(3), 1887.

[8] P. Krehl. *History of Shock Waves*, volume 1. Elsevier Inc., 2004.

[9] R. Becker. Stosswelle und detonation. *Zeitschrift für Physik*, Vol. 8(1):321–362, 1922.

[10] D. L. Chapman. VI. On the rate of explosion in gases. *The London, Edinburgh, and Dublin Philosophical Magazine and Journal of Science*, Vol. 47(284):90–104, 1899.

[11] E. Jouget. Sur la propagation des réactions chimiques dans les gaz. *Journal de Mathématiques Pures et Appliquées*, Vol. 1:347–425, 1905.

[12] F. G. Friedlander. The diffraction of sound pulses I. Diffraction by a semi-infinite plane. *Proceedings of the Royal Society A*, Vol. 186:322–344, 1946.

[13] P. O. K. Krehl. *History of Shock Waves, Explosions and Impact A Chronological and Biographical Reference*. Springer-Verlag Berlin Heidelberg, 2009.

[14] L. S. García-Colín, R. M. Velasco, and F. J. Uribe. Beyond the Navier-Stokes equations: Burnett hydrodynamics. *Physics reports*, Vol. 465:149–189, 2008.

[15] G. Bird. The velocity distribution function within a shock wave. *Journal of Fluid Mechanics*, Vol. 30(3):479–487, 1967.

[16] M. Morduchow and P. A. Libby. On a complete solution of the one-dimensional flow equations of a viscous, heat-conducting, compressible gas. *Journal of the Aeronautical Sciences*, Vol. 16(11):674–704, 1949.

[17] G. C. Pham-Van-Diep, D. A. Erwin, and E.P. Muntz. Testing continuum descriptions of low-Mach-number shock structures. *Journal of Fluid Mechanics*, Vol. 232:403–413, 1991.

[18] K. A. Fisco and D. R. Chapman. Comparison of Burnett, super-Burnett and Monte Carlo solutions for hypersonic shock structure. In E. P. Muntz, D. P. Weaver, and D. H. Campbell, editors, *Rarefied Gas Dynamics: Theoretical and Computational Techniques*, volume 18, pages 374–395. AIAA, Washington, DC, 1989.

[19] E. F. Toro. *Riemann Solvers and Numerical Methods for Fluid Dynamics*. Springer-Verlag Berlin Heidelberg, 3rd edition, 2009.

[20] G. Jiang and C. Shu. Efficient implementation of weighted ENO schemes. *Journal of Computational Physics*, Vol. 126:202–228, 1996.

[21] M. R. Betney, B. Tully, N. A. Hawker, and Y. Ventikos. Computational modelling of the interaction of shock waves with multiple gas-filled bubbles in a liquid. *Physics of fluids*, Vol. 27:036101, 2015.

[22] V. Nguyen, T. Phan, and W. Park. Numerical modeling of multiphase compressible flows with the presence of shock waves using an interface-sharpening five-equation model. *International Journal of Multiphase Flow*, Vol. 135:103542, 2021.

[23] D. H. Tsai and C. W. Beckett. Shock wave propagation in cubic lattices. *Journal of Geophysical Research*, Vol. 71(10):2601–2608, 1966.

[24] B. L. Holian. Atomistic computer simulations of shock waves. *Shock Waves*, Vol. 5(3):149–157, 1995.

[25] W. G. Hoover. Structure of a shock-wave front in a liquid. *Physical Review Letters*, Vol. 42(23):1531–1534, 1979.

[26] B. L. Holian, W. G. Hoover, B. Moran, and G. K. Straub. Shock-wave structure via nonequilibrium molecular dynamics and Navier-Stokes continuum mechanics. *Physical Review A*, Vol. 22:2798–2808, 1980.

[27] E. Salomons and M. Mareschal. Usefulness of the Burnett description of strong shock waves. *Physical Review Letters*, Vol. 69(2):269–272, 1992.

[28] B. L. Holian, C. W. Patterson, M. Mareschal, and E. Salomons. Modeling shock waves in an ideal gas: Going beyond the Navier-Stokes level. *Physical Review E*, Vol. 47(1):R24–R27, 1993.

[29] S. K. Kannam, B. D. Todd, J. S. Hansen, and P. J. Daivis. Slip length of water on graphene: Limitations of non-equilibrium molecular dynamics simulations. *The Journal of Chemical Physics*, Vol. 136:024705, 2012.

[30] B. Hafskjold, D. Bedeaux, Ø. Wilhelmsen, and S. Kjelstrup. Theory and simulation of shock waves: Entropy production and energy conversion. *Physical Review E*, Vol. 104:014131, 2021.

[31] T. van Westen, M. Hammer, B. Hafskjold, A. Aasen, J. Gross, and Ø. Wilhelmsen. Perturbation theories for fluids with short-ranged attractive forces: A case study of the Lennard-Jones spline fluid. Under review, 2022.

[32] Ø. Wilhelmsen, A. Aasen, G. Skaugen, P. Aursand, A. Austegard, E. Aursand, M. Gjennestad, H. Lund, G. Linga, and M. Hammer. Thermodynamic modeling with equations of state: Present challenges with established methods. *Industrial Engineering Chemistry Research*, Vol. 56(13):3503–3515, 2017.

[33] P. W. Zitzewitz, R. F. Neff, and M. Davids. *Physics: principles and problems*. Glencoe/McGraw-Hill, 1st edition, 1995.

[34] G. S. K. Wong and S. Zhu. Speed of sound in seawater as a function of salinity, temperature, and pressure. *The Journal of the Acoustical Society of America*, Vol. 97(3):1732, 1995.

[35] S. Kjelstrup and D. Bedeaux. *Non-Equilibrium Thermodynamics of heterogeneous systems*, volume 16. World scientific Publishing, 2008.

[36] B. Bird, S. Stewart, and E. W. Lightfoot. *Transport Phenomena*. Hamilton Printing, 2nd edition, 2002.

[37] S. Bhola and T. K. Sengupta. Roles of bulk viscosity on transonic shock-wave/boundary layer interactions. *Physics of Fluids*, Vol. 31:085115, 2019.

[38] H. A. Jackobsen. *Chemical Reactor Modeling*. Springer International Publishing AG, 2nd edition, 2014.

[39] S. T. Munkejord. *Analysis of the two-fluid model and the drift-flux model for numerical calculation of two-phase flow*. PhD thesis, NTNU, 2006.

[40] L. Petzold. Automatic selection of methods for solving stiff and nonstiff systems of ordinary differential equations. *SIAM Journal on Scientific and Statistical Computing*, Vol. 4(1):136–147, 1983.

[41] P. Birken, G. Gassner, M. Haas, and C. Munz. Efficient time integration for discontinuous galerkin methods for the unsteady 3D Navier-Stokes equations. In *European Congress on Computational Methods in Applied Sciences and Engineering (ECCOMAS 2012)*.

[42] E. Johannessen and D. Bedeaux. The nonequilibrium Van der Waals square gradient model.(II). local equillibrium of the Gibbs surface. *Physica A*, Vol. 330:354–372, 2003.

[43] J. A. Barker and D. Henderson. Pertubation theory and equation of state for fluids: The square-well potential. *The Journal of Chemical Physics*, Vol. 47(8):2856–2861, 1967.

[44] C. G. Gray and K. E. Gubbins. *Theory of molecular fluids*. Oxford University Press, New york, 1st edition, 1985.

[45] J. P. Hansen and I. R. McDonald. *Theory of simple liquids*. Academic Press, London, 3rd edition, 2006.

[46] D. Ben-Amotz and G. Stell. Reformulation of Weeks-Chandler-Andersen perturbation theory directly in terms of a hard-sphere reference system. *Journal of Physical Chemistry B*, Vol. 108(21):6877–6882, 2004.

[47] N. F. Carnahan and K. E. Starling. Equation of state for nonattracting rigid spheres. *Journal of Chemical Physics*, Vol. 51:635–636, 1969.

[48] E. W. Lemmon and R. T. Jacobsen. Viscosity and thermal conductivity equations for nitrogen, oxygen, argon, and air. *International Journal of Thermophysics*, Vol. 25(1):21–69, 2004.

[49] G. G. Stokes. On the theories of the internal friction of fluids in motion, and the equillibrium and motion of elastic solids. *Cambridge Philosophical Society*, Vol. 8:287–319, 1845.

[50] R. S. Chatwell and J. Vrabec. Bulk viscosity of liquid noble gases. *Journal of Chemical Physics*, Vol. 152:094503, 2020.

[51] S. R. De Groot and P. Mazur. *Non-Equilibrium Thermodynamics*. North Holland Publishing Company - Amsterdam, 1st edition, 1962.

[52] D. J. Evans and G. P. Morriss. *Statistical Mechanics of Nonequillibrium Liquids*. Academic Press, London, 2nd edition, 1990.

[53] V. A. Titarev and E. F. Toro. Musta schemes for multi-dimensional hyperbolic systems: analysis and improvements. *International Journal for Numerical Methods in Fluids*, Vol. 49(2):117–147, 2005.

[54] Y. Shen, G. Zha, and X. Chen. High order conservative differencing for viscous terms and the application to vortex-induced vibration flows. *Journal of computational physics*, Vol. 228(22):8283–8300, 2009.

[55] M. Abramowitz and I. A. Stegun. *Handbook of Mathematical Functions with Formulas, Graphs, and Mathematical Tables*. Dover Publications, 9th edition, 1972.

[56] P. Virtanen, R. Gommers, T. E. Oliphant, M. Haberland, T. Reddy, , D. Cournapeau, E. Burovski, P. Peterson, W. Weckesser, J. Bright, S. J. van der Walt, M. Brett, J. Wilson, K. J. Millman, N. Mayorov, A. R. J. Nelson, E. Jones, R. Kern, E. Larson, C. J. Carey, İ. Polat, Y. Feng, E. W. Moore, J. VanderPlas, D. Laxalde, J. Perktold, R. Cimrman, I. Henriksen, E. A. Quintero, C. R. Harris, A. M. Archibald, A. H. Ribeiro, F. Pedregosa, P. van Mulbregt, and SciPy 1.0 Contributors. SciPy 1.0: Fundamental Algorithms for Scientific Computing in Python. *Nature Methods*, 17:261–272, 2020.

[57] J. R. Dormand and P. J. Prince. A family of embedded Runge-Kutta formulae. *Comptes rendus de l'Académie des Sciences*, Vol. 6(1):19–26, 1980.

[58] D. Frenkel and B. Smit. *Understanding Molecular Simulation*. Academic Press, 2nd edition, 1996.

[59] K. R. Kristiansen. Transport properties of the simple Lennard-Jones/spline fluid I: Binary scattering and high-accuracy low-density transport coefficients. *Frontiers in Physics*, Vol. 8:271, 2020.

[60] D. G. Altman and J. M. Bland. Standard deviations and standard errors. *The BMJ*, Vol. 331:903, 2005.

Appendix A

A.1 Finite volume method

The purpose of this section is to use the finite volume method to discretize the Euler equations in space. By defining the volume average $Q = Q(x,t)$ of a conserved quantity Q at time $t = t_1$ and x within the range $[x_{1-1/2}, x_{1+1/2}]$ we get:

$$\overline{Q}(t_1) = \frac{1}{x_{i+1/2} - x_{1-1/2}} \int_{x_{i-1/2}}^{x_{i+1/2}} Q(x,t_1)dx \tag{A.1}$$

Doing the same for $t = t_2$, we can the integrate in time on the form

$$Q_i(x,t_2) = Q(x,t_1) - \int_{t_1}^{t_2} \frac{\partial f}{\partial x} dt \tag{A.2}$$

Where f is the flux. To obtain the volume average at t_2 we then integrate over the cell volume and divide the result by $\Delta x_i = x_{i+1/2} - x_{i-1/2}$ i.e.

$$\overline{Q}_i(t_2) = \frac{1}{\Delta x_i} \int_{x_{i-1/2}}^{x_{i+1/2}} \left(Q(x,t_1) - \int_{t_1}^{t_2} \frac{\partial f}{\partial x} dt \right) dx \tag{A.3}$$

By then applying the divergence theorem we can substitute the volume integral with values of $f(x)$ evaluated at the surface i.e. the edges $(x_{1-1/2}, x_{1+1/2})$:

$$\overline{Q}_i(t_2) = \overline{Q}(t_1) - \frac{1}{\Delta x_i} \left(\int_{t_1}^{t_2} \frac{\partial f_{i+1/2}}{\partial x} dt - \int_{t_1}^{t_2} \frac{\partial f_{i-1/2}}{\partial x} dt \right) \tag{A.4}$$

Differentiating with respect to time we then obtain the required equation:

$$\frac{\partial \overline{Q}_i}{\partial t} = -\frac{F_{i+1/2} - F_{i-1/2}}{\Delta x_i} \tag{A.5}$$

Note that we applied central differences to the derivatives within the diffusive flux in order to utilize the equation.

A.2 List of reduced variables

The results from Navier-Stokes equations and computations using the equation of state were converted into dimensionless Lennard-Jones units by using Table A.1. The characteristic mass was the mass of an argon particle, the characteristic energy ϵ/k was 124 K, and the characteristic length was $\sigma = 3.418\mathring{A}$.

Symbol	LJ Unit	Definition
$\mathbf{J}_q^*$	$\mathbf{J}_q \frac{\sigma^3}{\epsilon} \left(\frac{m_1}{\epsilon}\right)^{1/2}$	Heat flux
$\mathbf{J}_q'^*$	$\mathbf{J}'_q \frac{\sigma^3}{\epsilon} \left(\frac{m_1}{\epsilon}\right)^{1/2}$	Measurable heat flux
$j^*, \mathbf{J}_m^*$	$\mathbf{J}_m \frac{\sigma^3}{(m_1\epsilon)^{1/2}}$	Mass flux
$\mathbf{J}_s^*$	$\mathbf{J}_s \frac{\sigma^3}{k} \left(\frac{m_1}{\epsilon}\right)^{1/2}$	Entropy flux
m^*	$\frac{m}{m_1}$	Mass
l^*	$\frac{l}{\sigma}$	Shock position
p^*, P_{xx}^*, Π^*	$\frac{p\sigma^3}{\epsilon}$	Pressure, pressure tensor, viscous pressure tensor
r^*, r_{ij}^*	$\frac{r}{\sigma}$	Radius, length between particle i and j
s^*	$s\frac{m_1}{k}$	Specific entropy
T^*	$\frac{k_b T}{\epsilon}$	Temperature
t^*	$\frac{t}{\sigma}\left(\frac{\epsilon}{m_1}\right)^{1/2}$	Time
u^*, u_{pot}^*, h^*	$u\frac{m_1}{\epsilon}, h\frac{m_1}{\epsilon}$	Specific internal and potential energy, specific enthalphy
V^*	$\frac{V}{\sigma^3}$	Volume
$\mathbf{v}^*$	$\mathbf{v}\left(\frac{m_1}{\epsilon}\right)^{1/2}$	Velocity
x^*	$\frac{x}{\sigma}$	Distance
η, ζ	$\frac{\eta\sigma^2}{(m_1\epsilon)^{\frac{1}{2}}}, \frac{\zeta\sigma^2}{(m_1\epsilon)^{\frac{1}{2}}}$	Shear viscosity, bulk viscosity
λ^*	$\lambda\frac{\sigma^2}{k}\left(\frac{m}{\epsilon}\right)^{1/2}$	Conductivity
ρ^*	$\rho\sigma^3$	Density
ρ^{s*}	$\rho^s\sigma^2$	Excess density
ρ_s	$\rho_s\frac{\sigma^3}{k}$	Entropy density
ρ_s^s	$\rho_s^{s*} = \rho_s^s\frac{\sigma^2}{k}$	Excess entropy density
σ_s	$\sigma_s^* = \sigma\frac{\sigma^4}{k_b}\left(\frac{m_1}{\epsilon}\right)^{1/2}$	Local entropy production

Table A.1: Symbol list and definitions of variables in reduced Lennard-Jones units.

A.3 General Description of programs used

There were four major Python programs and two Fortran programs used to simulate a shock wave and derive the shock wave properties.

Starting with `eulerFast.py`. This was the program used to model the shock wave with the Navier-Stokes equations. The program runs through the terminal, requesting equilibriumm and shock temperature, and would model a shock wave for an inviscid or viscid fluid. After the shock was modelled ot would then compute the values to reduced LJ/s units and save them to .txt files.

The Fortran programs `nemd` and `annemd` performed the NEMD simulations and computed NEMD values. The program `nemd` would take an input file and run a speci-

fied simulation, which would be the equilibrium simulation, activation of shock and NVE simulation of the blast. Then the `annemd` program would take the output of `nemd` and compute the properties given in Section 2.2 and save it to a .DAT file named CPROPS.

The programs `motherGoose.py` and `fileRead.py` computes the shock wave properties. `motherGoose.py` reads the information from the NEMD- and N-S data then computes shock wave properties and entropy productions using functions written in `fileRead.py`.

Lastly we have `deviationGoose.py` which computes the error bars for the shock wave properties. It reads the information from the NEMD- data then computes shock wave properties and entropy productions using functions written in `fileRead.py` for each NEMD parallel saving the errors to .txt files. The programs that were implemented as part of this thesis work and can be found as supplementary material. Note that to run the Python code one needs to have the module Thermopack installed with the new LJ/s EOS.

A.4 Computing averages and Error bars

For the NEMD simulation data we utilize averages and error bars which are computed using the equations given in this section. The averages are computed as the arithmetic mean on the form:

$$\overline{x} = \frac{1}{N}\sum_{i=1}^{N} x_i \tag{A.6}$$

where N is the total number of parallels and the subscript i represents data from a parallel. Using the average we compute the standard deviation as:

$$\sigma_{SD} = \sqrt{\frac{1}{N}\sum_{i=1}^{n}\left(x_i - \overline{x}\right)^2} \tag{A.7}$$

With the standard error [60] we computed the error bars as three times the standard error i.e.

$$\text{SE} = \frac{3\sigma_{SD}}{\sqrt{N}} \tag{A.8}$$

These properties were computed for all properties in NEMD, in addition to the shock properties of each parallel.

A.5 Extrapolated bulk properties

The extrapolation of σ_q were not included in the discussion of the GEM method, but have been included here to show that σ_q did not affect the excess entropy production to a significant degree. The extrapolation of σ_q which can be shown in Figure A.1 where both methods compute a up- and downstream bulk close to zero.

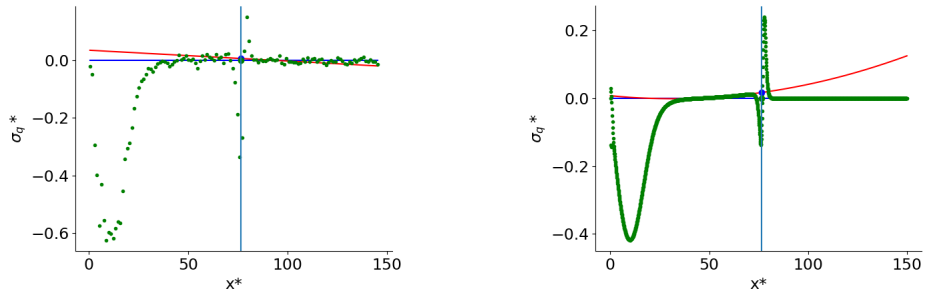

(a) NEMD.

(b) N-S.

Figure A.1: The method used for upstream and downstream properties for σ_q at $t^* = 6.25$. The red line is the upstream extrapolated bulk, the blue axis line is the surface of discontinuity. The red line is the extrapolated downstream bulk density.

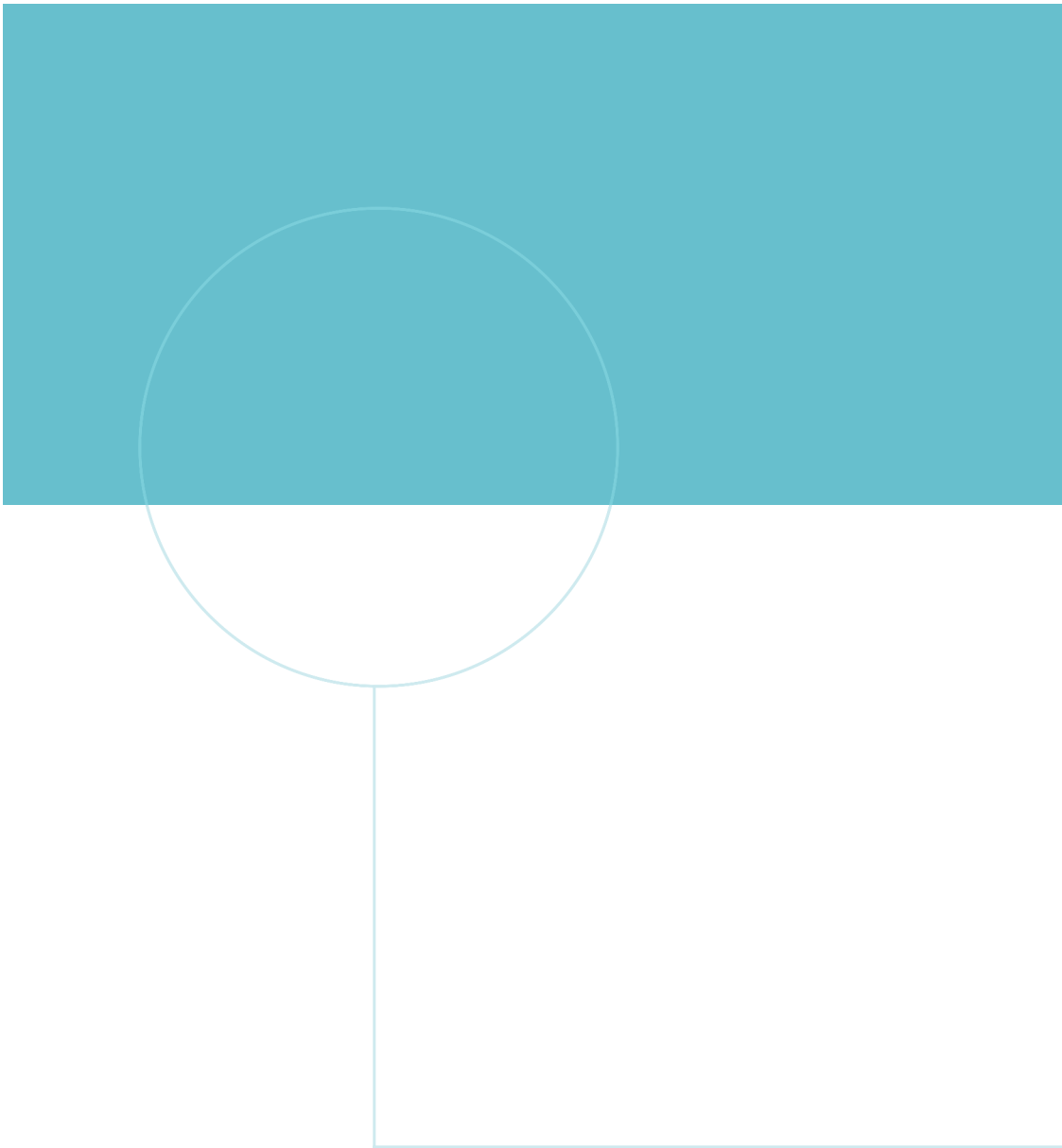

NTNU

Kunnskap for en bedre verden